

nnMIL: A generalizable multiple instance learning framework for computational pathology

Xiangde Luo¹, Jinxi Xiang¹, Yuanfeng Ji¹, Ruijiang Li^{*1,2}

¹*Department of Radiation Oncology, Stanford University School of Medicine, Stanford, CA, USA.*

²*Stanford Institute for Human-Centered Artificial Intelligence, Stanford, CA, USA*

** Correspondence to Ruijiang Li (rli2@stanford.edu).*

Funding. This study was supported in part by the National Institutes of Health under research grants R01CA269559, R01CA285456 and R01CA290715 from the National Cancer Institute.

arXiv:2511.14907v1 [cs.CV] 18 Nov 2025

Abstract

Computational pathology holds substantial promise for improving diagnosis and guiding treatment decisions. Recent pathology foundation models enable the extraction of rich patch-level representations from large-scale whole-slide images (WSIs), but current approaches for aggregating these features into slide-level predictions remain constrained by design limitations that hinder generalizability and reliability. Here we present **nnMIL**, a simple yet broadly applicable multiple-instance learning framework that connects patch-level foundation models to robust slide-level clinical inference. nnMIL introduces random sampling at both the patch and feature levels, enabling large-batch optimization, task-aware sampling strategies, and efficient and scalable training across datasets and model architectures. A lightweight aggregator performs sliding-window inference to generate ensemble slide-level predictions and supports principled uncertainty estimation. Across 40,000 WSIs encompassing 35 clinical tasks and four pathology foundation models, nnMIL consistently outperformed existing MIL methods for disease diagnosis, histologic subtyping, molecular biomarker detection, and pan-cancer prognosis prediction. It further demonstrated strong cross-model generalization, reliable uncertainty quantification, and robust survival stratification in multiple external cohorts. In conclusion, nnMIL offers a practical and generalizable solution for translating pathology foundation models into clinically meaningful predictions, advancing the development and deployment of reliable AI systems in real-world settings.

Source codes: <https://github.com/Luoxd1996/nnMIL>

Introduction

Histopathology is the gold standard for disease diagnosis and provides valuable information for informing prognosis and treatment decisions¹⁻⁴. Recent advances in computational pathology and the advent of pathology foundation models have enabled powerful patch-level feature representations learned from large-scale whole-slide images (WSIs)⁵⁻¹³. These foundation models have shown strong diagnostic performance and generalization across diverse tissue types¹⁴⁻¹⁶. However, translating patch-level representations into slide-level predictions remains challenging, particularly when clinical deployment requires both performance and reliability¹⁷.

Multiple instance learning (MIL) has become the standard paradigm for aggregating patch-level representations into a slide-level prediction, providing a crucial link between foundation model embeddings and downstream clinical applications^{18,19}. Because the number of patches is highly variable across WSIs, existing MIL methods are limited to a batch size of one for training¹⁸⁻²⁴. This constraint precludes advanced optimization strategies and impedes model convergence²⁵. Although recent attention- and transformer-based variants of MIL have shown modest performance gains, they largely focus on architectural refinements for specific applications rather than addressing the fundamental issues of generalizability and robustness^{17,25-28}.

Beyond architectural considerations, progress in MIL has also been shaped by training procedures. Multiple studies have reported substantial performance variability even using the same MIL architecture^{17,25,26,29,30}. In general machine learning, batch construction, sampling strategy, loss formulation, and optimization heuristics all have a significant impact on model performance, and in some cases more so than architectural choices themselves^{31,32}. Despite their importance, these components have received little systematic analysis: making their true impact difficult to assess and hindering the development of a unified, generalizable training recipe for MIL.

Here, *we propose a training-centric perspective that focuses on efficient training in the foundation-model era, rather than MIL network design*. We systematically investigate MIL training strategies and distill them into nnMIL, a simple yet generalizable framework that unifies patch-level foundation-model embeddings with stable and scalable slide-level learning. nnMIL resolves the long-standing limitation of single-batch training by introducing patch sampling, which converts variable-length bags into fixed-length sub-bags and enables large-batch optimization using balanced mini-batches. For slide-level aggregation, nnMIL employs a sliding-window scheme that integrates predictions from multiple overlapping sub-sampled embeddings, effectively functioning as an ensemble and providing principled uncertainty estimates for model outputs^{33,34}. Furthermore, nnMIL offers a plug-and-play performance enhancement that is compatible with most existing MIL networks, underscoring its extensibility and value for future methodological developments.

Comprehensive evaluation and benchmarking across 35 clinically relevant tasks using nearly 40,000 WSIs demonstrates that nnMIL consistently outperforms existing MIL methods in disease diagnosis and subtyping, molecular biomarker detection, and pan-cancer prognosis prediction, regardless of the pathology foundation models used for feature extraction. Beyond its strong performance, nnMIL provides quantification of model confidence by computing uncertainty scores of the output, which substantially improves accuracy among low-uncertainty cases while reserving cases with the highest uncertainty for selective referral in disease diagnosis. For prognosis prediction, the uncertainty scores can be used to further refine survival stratification within the high-risk population. By systematically optimizing the configuration of multiple instance learning, nnMIL establishes a versatile framework for solving clinically relevant tasks in computational pathology.

Results

Overview of nnMIL

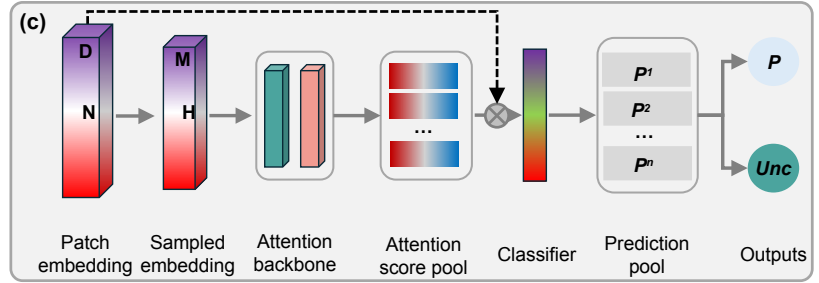
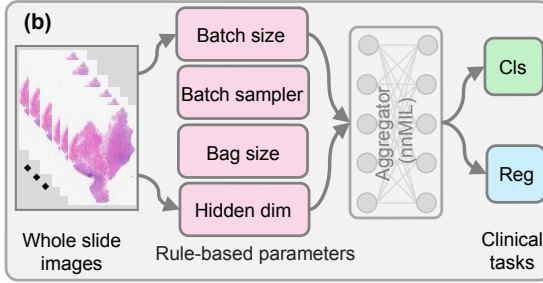
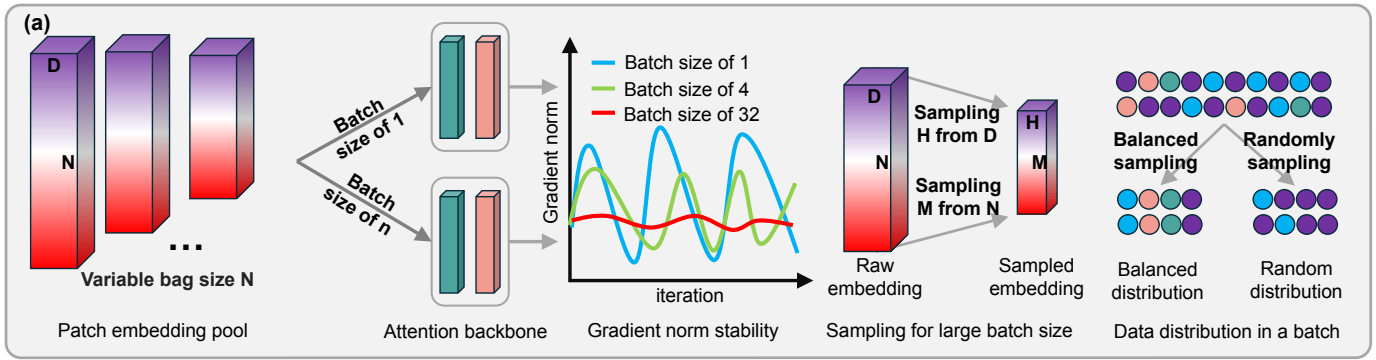
We developed nnMIL, a simple yet generalizable framework for multiple instance learning (MIL) designed to bridge the gap between patch-level foundation models and slide-level clinical prediction (**Figure 1**). The framework operates on patch features extracted from any pathology foundation models (such as GigaPath⁵, UNI⁹, H-Optimus-0/H0⁸ or Virchow2³⁷) and trains a slide-level aggregator for task-specific prediction. To address a long-standing problem in MIL, where training is constrained by a batch size of one due to varying bag sizes (i.e., number of patches) across WSIs, we redesigned the training pipeline to enable efficient large-batch optimization. By introducing patch sampling, nnMIL partitions variable-length bags into fixed-length sub-bags, thereby supporting substantially larger and more balanced batch sizes. Furthermore, a task-specific batch sampler was developed to improve data utilization across different tasks, collectively enhancing training efficiency, stability, and overall performance. Finally, we designed the slide-level aggregator such that it preserves the semantic integrity of pretrained features by learning from a subset of embeddings and predicts across the entire feature embedding space via a sliding-window inference scheme. This provides ensemble predictions, allowing estimation of the uncertainty in model outputs.

We evaluated and benchmarked nnMIL across 35 computational pathology tasks using nearly 40,000 unique whole-slide images (WSIs) across four pathology foundation models. The results demonstrate that nnMIL consistently outperforms existing MIL methods across all foundation models^{18,20–24}. Further, nnMIL yields model uncertainty estimates that align well with actual reliability, enhancing the clinical utility of slide-level predictions.

Disease diagnosis and subtyping

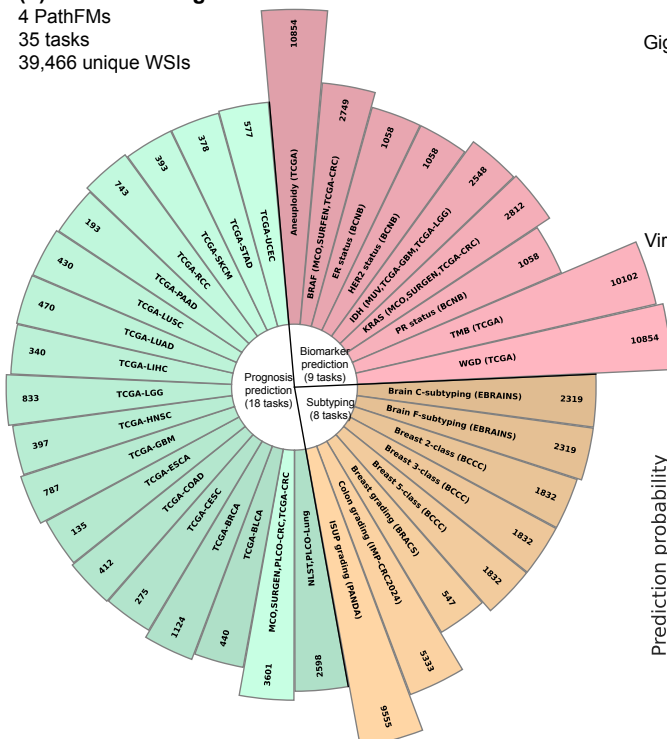
Accurate disease classification and subtyping are fundamental tasks in computational pathology, providing crucial information for diagnosis, treatment selection, and prognosis assessment. We conducted benchmark experiments on eight challenging disease classification and subtyping tasks, including skin cancer subtyping (2 cls, 3 cls, and 5 cls, cls means classes) using the Basal Cell Carcinoma Classification (BCCC) dataset³⁸ (1,832 samples), breast cancer subtyping (7 cls) using the BReAst Carcinoma Subtyping (BRACS) dataset (547 samples)³⁹, brain tumour subtyping (12 cls and 30 cls) using the EBRAINS dataset (2,319 samples)⁴⁰, colorectal cancer diagnosis using IMP-CRS2024 (5,333 samples)⁴¹ and Gleason grading of prostate cancer using PANDA (9,555 samples)⁴². For a fair comparison, we used the official or widely adopted data splits for model training and validation.

Averaged over eight subtyping tasks, nnMIL achieved the best overall performance among all evaluated



(d) Benchmarking:

4 PathFMs
35 tasks
39,466 unique WSIs



(e)

Overall ranking → Best Worst

	nnMIL	ABMIL	DSMIL	DTFD	TransMIL	WIKG	ILRA
GigaPath	1.68 ±1.81	3.90 ±3.43	3.65 ±2.69	3.85 ±3.26	4.70 ±2.88	4.47 ±3.38	5.72 ±1.68
H0	1.88 ±1.55	3.55 ±2.66	3.85 ±2.80	3.62 ±3.11	4.38 ±3.68	4.95 ±2.82	5.69 ±3.17
UNI	1.75 ±1.37	3.40 ±2.81	4.10 ±2.09	4.05 ±3.33	4.20 ±3.81	4.70 ±2.83	5.77 ±3.08
Virchow2	1.35 ±0.44	3.83 ±1.74	3.85 ±2.80	4.00 ±3.28	4.35 ±2.64	4.58 ±3.07	6.00 ±2.89
Mean	1.66 ±1.29	3.67 ±2.66	3.86 ±2.60	3.88 ±3.25	4.41 ±3.25	4.67 ±3.03	5.79 ±2.70

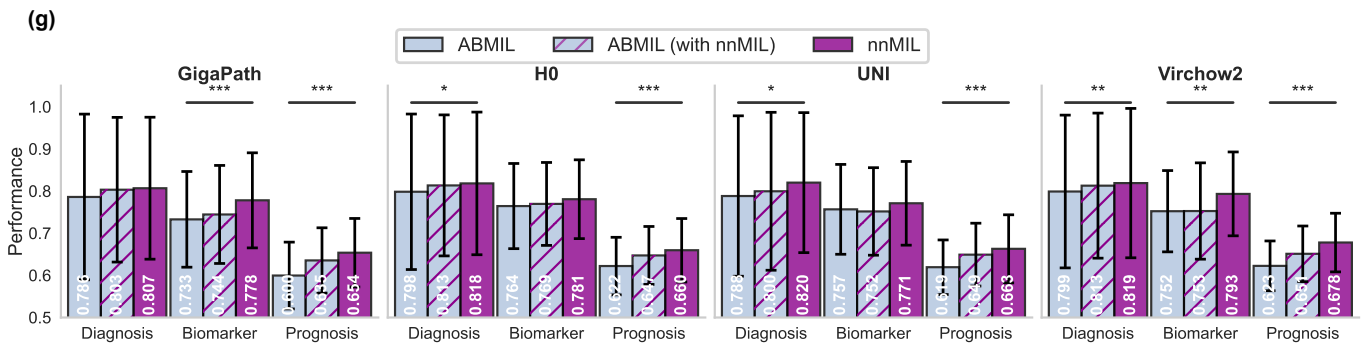
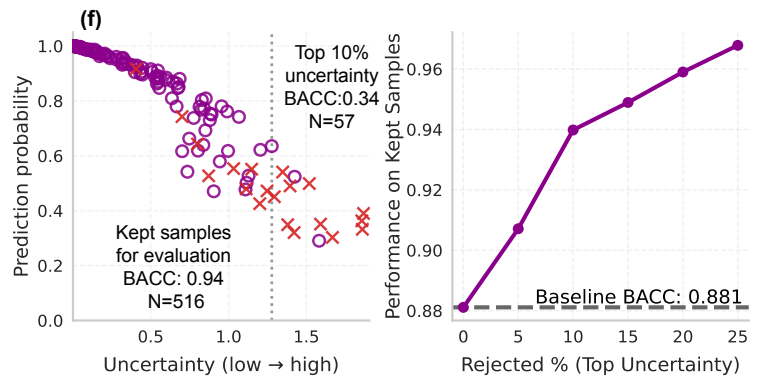


Figure 1: Overview of nnMIL framework and evaluation. nnMIL is a generalizable multiple instance learning framework that shows superior performance across 35 slide-level computational pathology tasks. **(a)**, The motivation of nnMIL is to enable MIL training in a *simple yet generalizable* manner. We realize this idea by leveraging large-batch optimization to enhance both robustness and effectiveness of model training^{35,36}. Specifically, we introduce stochastic sampling at both the patch level (randomly sampling M out of N patches) and the feature level (randomly sampling H out of D embedding dimensions), combined with task-aware batch construction tailored for MIL optimization. **(b)** A rule-based parameterization strategy, determined according to dataset characteristics, is further employed to simplify and streamline both training and inference. **(c)**, The simplified attention-based aggregator for slide-level prediction and uncertainty estimation. **(d)**, Overview of the evaluation datasets encompassing 35 slide-level clinical tasks across three major categories: disease classification and subtyping (8 tasks), molecular biomarker detection (12 tasks), and prognosis prediction (15 tasks). **(e)**, Overall ranking scores for MIL methods across all 35 slide-level clinical tasks and pathology foundation models (mean \pm standard deviation). **(f)**, Reliability analysis of model predictions based on uncertainty scores (Unc) in the left panel shows that removing cases with the highest uncertainty scores could improve model performance on disease diagnosis (BCCC 3 cls) in the right panel. **(g)**, Comparison among conventional ABMIL trained with a batch size of 1, ABMIL with nnMIL training strategies (larger batch size with patch-level sampling and task-aware sampling), and the complete nnMIL framework across four pathology foundation models (Virchow2, GigaPath, UNI, and H0). These results demonstrate that nnMIL improves performance and generalizability regardless of the pathology foundation models used for feature extraction. WSI: whole-slide image; PathFMs: pathology foundation models; *Cls*: classification; *Reg*: Regression; *P*: prediction; *Unc*: uncertainty; BACC: balanced accuracy.

MIL methods (**Figure 2 (a)**, **Extended Data Figure 1 (a)**, and **Extended Data Tables 1 to 4**). Compared with the second-best method, ABMIL¹⁸, nnMIL improved performance by 2.6–3.8% across four pathology foundation models. The increase in performance can be as large as 6.1% for UNI and 7.3% for GigaPath compared with ILRA. In addition, nnMIL exhibited a marked reduction in performance variance ($P < 0.001$), indicating greater stability across different cancer types. The overall performance of nnMIL was highly consistent across different pathology foundation models, falling within a narrow range of 80.7% and 82.0%. This indicates that nnMIL’s advantage is model-agnostic and independent of any specific feature extractors.

Among all MIL methods, nnMIL ranked first on five tasks, second on two, and fourth on one, reflecting strong performance in diagnosing diverse diseases (**Figure 2 (b)-(i)**). Compared with the second-best method, ABMIL, nnMIL achieved its largest gain on the EBRAINS Fine classification task with a 10.5% relative improvement in balanced accuracy (BA): 0.724 vs 0.656, $P < 0.001$, while showing a slight 1.5% decrease on the PANDA dataset (Kappa: 0.924 vs 0.938, $P < 0.001$). In the smallest subtyping dataset, BRACS, nnMIL achieved a BA of 0.447, representing an 8.8% relative improvement over DTFD with a BA of 0.411.

To assess the reliability of slide-level predictions, we further analyzed the relationship between model uncertainty and classification performance by conducting a selective prediction experiment through sample rejection (**Figure 2 (j)-(m)** and **Extended Data Figure 2 (a)**). As slides with the highest uncertainty scores were progressively excluded, nnMIL’s performance on the retained slides increased steadily across various

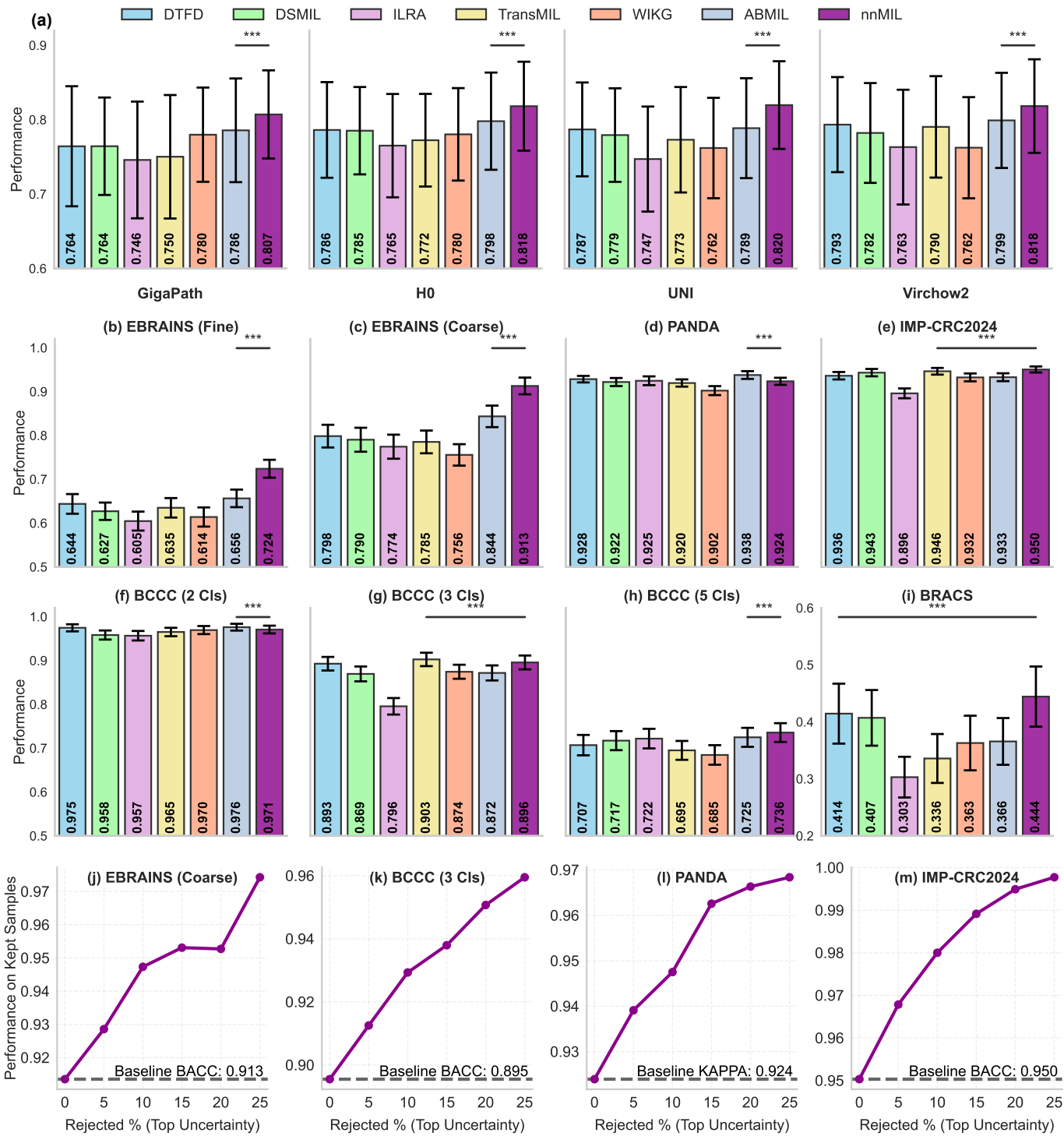


Figure 2: Disease classification and subtyping. (a), Comparisons of MIL methods for performance on 8 disease classification and subtyping tasks across four pathology foundation models (GigaPath, H0, UNI and Virchow2). nnMIL was compared with six widely used MIL methods including DTFD, DSMIL, ILRA, TransMIL, WIKG and ABMIL. (b)-(i), Comparison across eight individual tasks using UNI as the feature extractor, including EBRAINS (30 cls Fine and 12 cls Coarse tasks, where cls means classes), PANDA (7 cls), IMP-CRC2024 (3 cls), BCCC (2-, 3-, and 5-cls tasks), and BRACS (7 cls). Performance was evaluated using balanced accuracy (BACC), except for PANDA, which was assessed with Cohen’s Kappa. (j)-(m), Performance analysis after excluding cases with the highest uncertainty scores. Statistical significance was determined using a two-sided Wilcoxon signed-rank test, where * indicates $P < 0.05$, ** indicates $P < 0.01$, and *** indicates $P < 0.001$. All results are reported as mean \pm standard deviation, estimated from 1,000 bootstrap replicates.

tasks, suggesting that uncertainty estimates are well aligned with prediction reliability. For instance, excluding just 10% of the slides with the highest uncertainty scores achieved substantial error reduction by as much as 60% from 5.0% to 2.0% in the IMP-CRC2024 dataset. These results indicate that the uncertainty scores estimated by nnMIL can be used to identify complex cases with low-confidence model predictions, which allows selective referral for pathologist review, thereby further increasing overall diagnostic performance.

Molecular biomarker detection

Accurate prediction of protein expression or gene mutation from routine histopathology slides can accelerate treatment decisions and reduce unnecessary testing²⁷. In this study, we evaluated the ability of nnMIL and other MIL methods to predict molecular phenotypes from whole-slide histopathology images. Specifically, we conducted experiments on nine clinically relevant molecular biomarkers across 12 datasets, including three protein expression biomarkers (ER, PR, and HER2), three gene mutations (*BRAF*, *KRAS*, and *IDH*), and three pan-cancer genomic biomarkers (whole-genome doubling (WGD), tumour mutational burden (TMB), and aneuploidy). These biomarkers were derived from large-scale cohorts, including an early breast cancer core needle biopsy dataset (BCNB, 1,059 samples) containing PR, ER, and HER2 statuses⁴³; three colorectal cancer cohorts for *BRAF* and *KRAS* mutations (SURGEN⁴⁴ as the development set, $n = 799$; MCO^{45,46} and TCGA-CRC⁴⁷ as external evaluation sets, $n = 1,492$ and $n = 521$); three brain tumour cohorts for *IDH* mutation (MUV as the development set⁴⁰, $n = 872$; TCGA-GBM and TCGA-LGG as external evaluation sets⁴⁷, $n = 834$ and $n = 842$); and the pan-cancer TCGA dataset ($n = 10,854$) annotated with WGD, TMB, and aneuploidy statuses⁴⁸. These evaluation datasets and tasks provide a comprehensive benchmark for evaluating MIL methods for slide-level molecular prediction. All models were trained under identical bag-level supervision and compared across four pathology foundation models (Virchow2, GigaPath, UNI, and H0) to ensure fair comparison.

Averaged across all nine biomarkers, nnMIL consistently outperformed other MIL methods across four pathology foundation models (Virchow2, GigaPath, UNI, and H0). Specifically, nnMIL with Virchow2 as the feature extractor achieved the highest performance with a mean AUC of 0.795, surpassing ABMIL and DSMIL²¹ by 3.3–4.1% ($P < 0.001$) (**Figure 3 (a)**, **Extended Data Figure 1 (b)**, and **Extended Data Tables 5 to 8**). To further assess performance for individual biomarkers, we compared all MIL methods using Virchow2 as the feature extractor (**Figure 3 (b)-(m)**). For protein expression prediction, nnMIL significantly outperformed all competing approaches on ER, HER2, and PR in the BCNB dataset ($P < 0.001$). For gene mutation prediction (*BRAF*, *KRAS* and *IDH*), nnMIL ranked the first on four out of six external evaluation datasets. In addition, nnMIL outperformed all comparison methods in WGD and TMB prediction, achieving high AUCs of 0.845 and 0.876, respectively, and attained the second-best performance on aneuploidy prediction (Pearson’s $r = 0.630$ vs 0.637 for TransMIL²³). Collectively, these results highlight nnMIL’s ability to generalize across

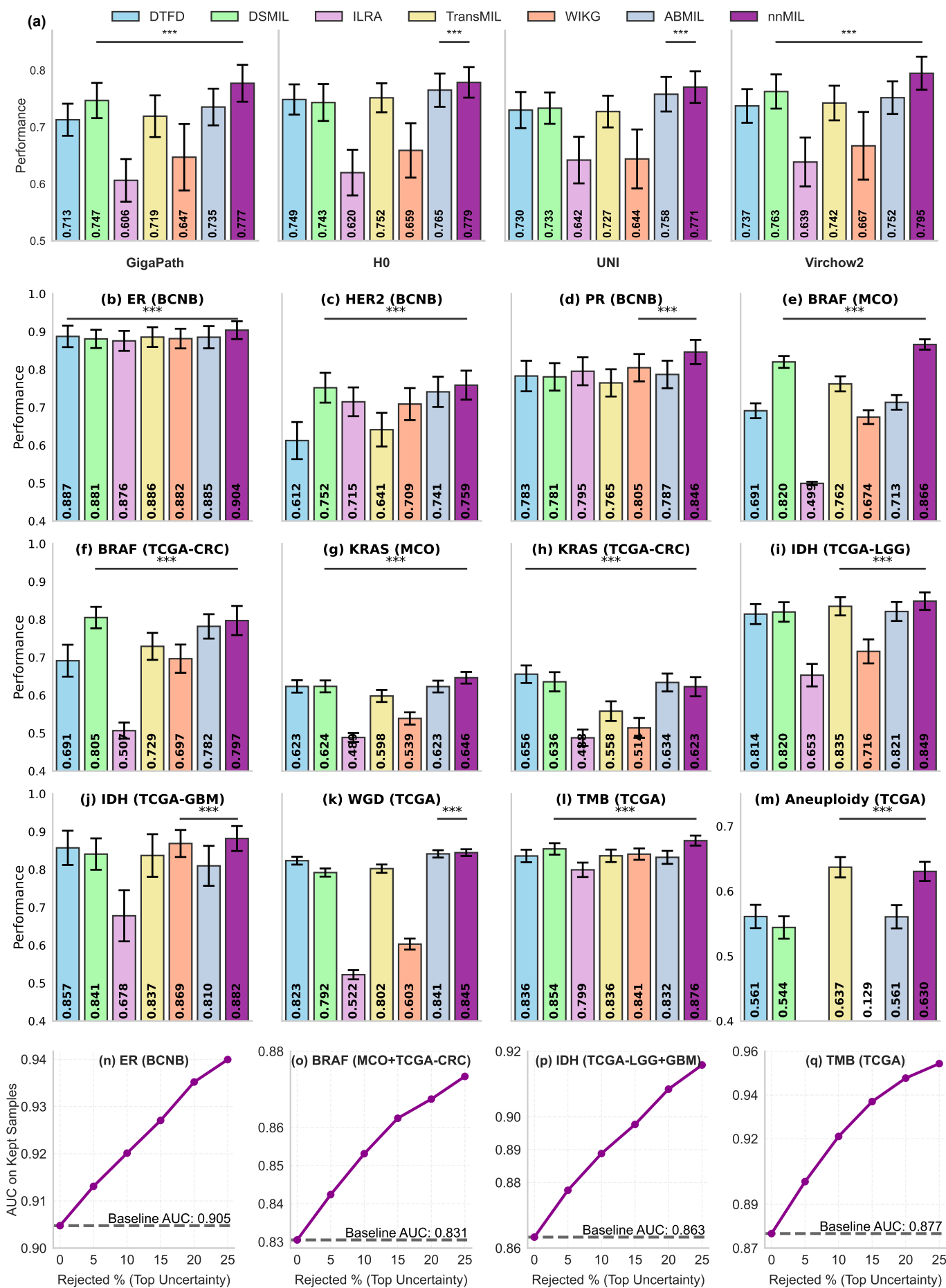


Figure 3: **Molecular biomarker detection.** (a), Average performance of nnMIL and comparative methods across 12 datasets representing 9 molecular biomarkers evaluated on four pathology foundation models (GigaPath, H0, UNI, and Virchow2). nnMIL was benchmarked against six widely used MIL methods, including DTFD, DSMIL, ILRA, TransMIL, WIKG, and ABMIL. (b)–(i), Comparisons across 12 individual datasets using Virchow2 as the feature extractor, covering three breast cancer biomarkers (ER, HER2, and PR) from the BCNB cohort; two colorectal cancer biomarkers (BRAF and KRAS) from the TCGA-CRC and MCO cohorts; one brain tumor biomarker (IDH) from the TCGA-LGG and TCGA-HGG cohorts; and three pan-cancer genomic biomarkers (WGD, TMB, and Aneuploidy) from TCGA. Performance was evaluated using the area under the curve (AUC), except for Aneuploidy, which was a regression task assessed using the Pearson correlation coefficient. (j)–(m), Performance analysis after excluding samples with the highest uncertainty scores from nnMIL. Statistical significance was determined using a two-sided Wilcoxon signed-rank test, where * indicates $P < 0.05$, ** indicates $P < 0.01$, and *** indicates $P < 0.001$. All results are reported as mean \pm standard deviation, estimated from 1,000 bootstrap replicates.

both expression- and genome-level biomarkers, linking histomorphological features to underlying molecular alterations.

To further evaluate the reliability of biomarker prediction, we investigated the relationship between model uncertainty and prediction accuracy across all biomarkers (**Figure 3 (n)-(q)** and **Extended Data Figure 2 (b)**). As slides with the highest uncertainty scores obtained from nnMIL were progressively excluded, performance improved monotonically, indicating that uncertainty estimates were closely aligned with prediction reliability. Removing the top 25% most-uncertain samples increased the mean AUC from 0.905 to 0.940 for ER prediction, from 0.832 to 0.873 for BRAF, and from 0.863 to 0.916 for IDH, while the pan-cancer TMB prediction improved from 0.877 to 0.954. These results demonstrate that nnMIL can accurately perform biomarker prediction for a majority of samples with high confidence while identifying low-confidence cases for further molecular testing.

Pan-cancer prognosis prediction

Accurate prediction of survival outcomes from routine whole-slide pathology images can enable personalized treatment. To evaluate the prognostic capability of nnMIL, we curated a pan-cancer cohort of 6,602 patients from The Cancer Genome Atlas (TCGA), comprising 7,927 diagnostic hematoxylin and eosin (H&E) whole-slide images with corresponding follow-up data⁴⁷. Following previous works⁷, we trained and evaluated nnMIL on each cancer type using five-fold cross-validation, with disease-specific survival as the clinical endpoint.

Across all 16 cancer types, nnMIL consistently outperformed existing multiple instance learning approaches (**Figure 4 (a)**, **Extended Data Figure 1 (c)**, and **Extended Data Tables 9 to 12**). When trained with Virchow2 as the feature extractor, nnMIL achieved the highest mean C-Index of 0.670, significantly outperforming the second-best model with DSMIL²¹ with C-Index of 0.625. nnMIL maintained stable prog-

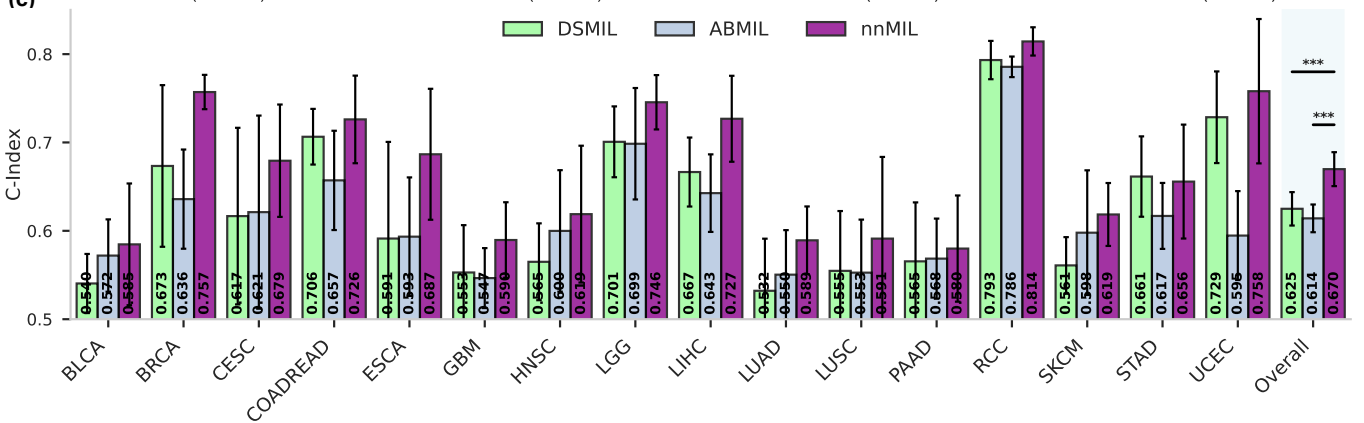
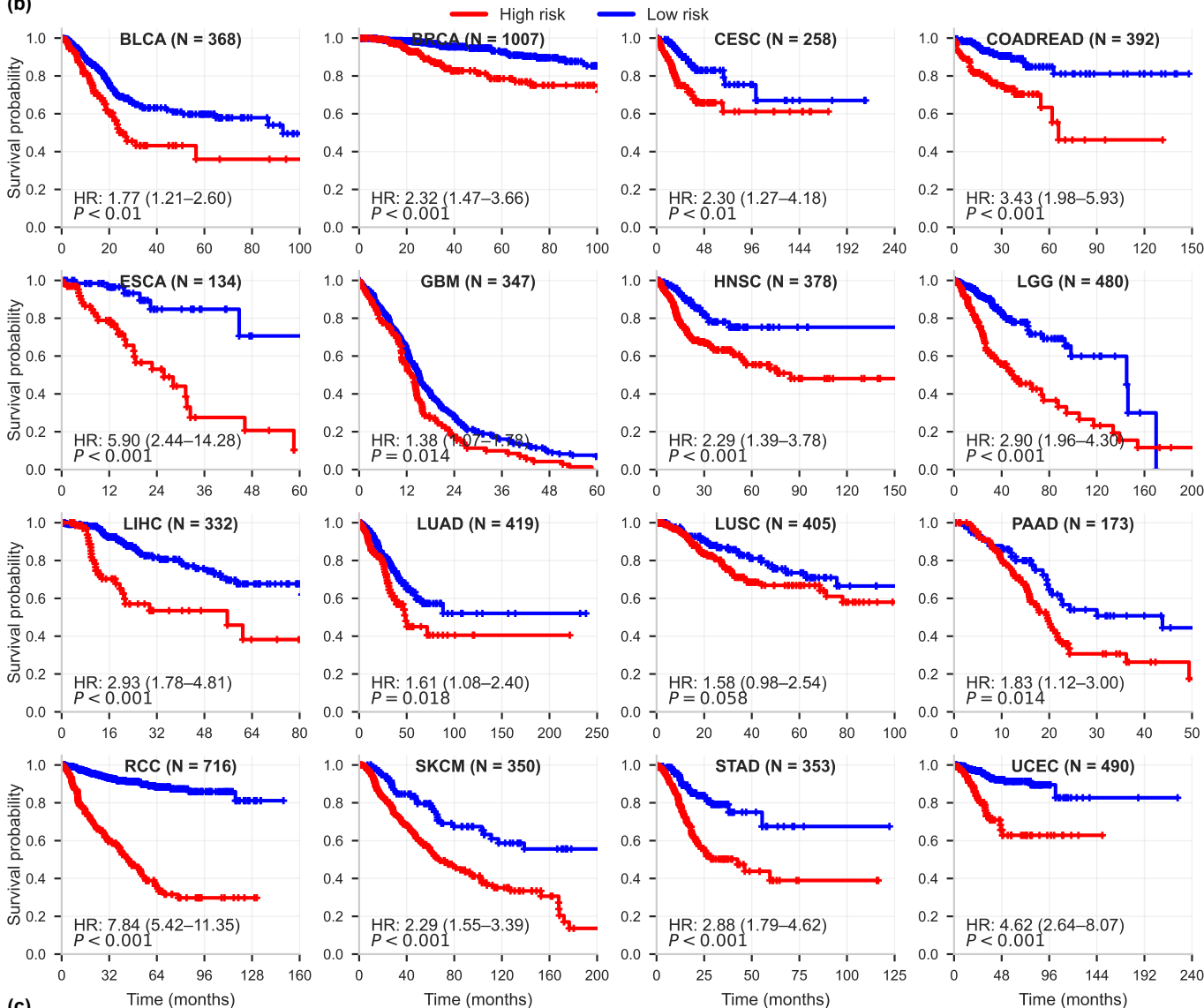
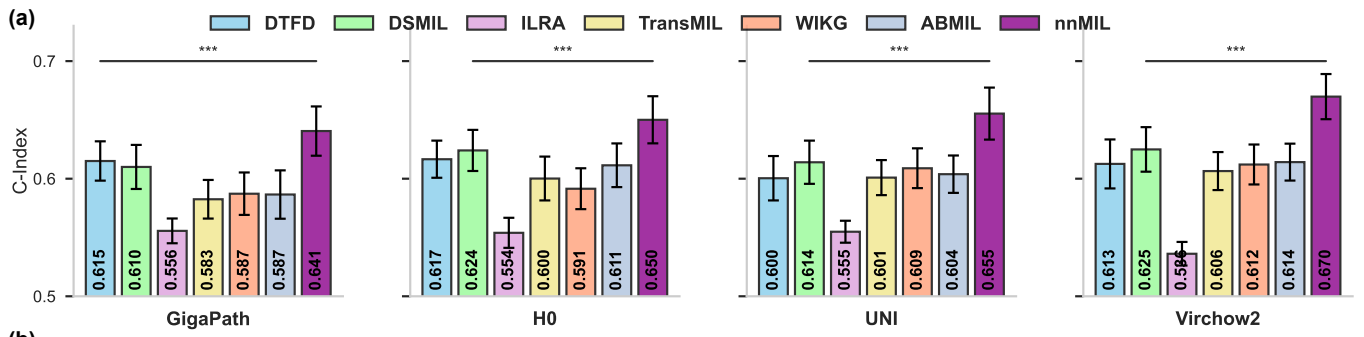


Figure 4: Pan-cancer prognosis prediction. (a), Average performance of nnMIL and comparative methods across 16 cancer types evaluated on four pathology foundation models (GigaPath, H0, UNI, and Virchow2). nnMIL was benchmarked against six widely used MIL methods, including DTFD, DSMIL, ILRA, TransMIL, WIKG, and ABMIL. (b), Kaplan–Meier survival plots (cut-off: median) of nnMIL across 16 cancer types using Virchow2 as the feature extractor, including bladder urothelial carcinoma (BLCA), breast invasive carcinoma (BRCA), cervical squamous cell carcinoma and endocervical adenocarcinoma (CESC), colorectal and rectal adenocarcinoma (COADREAD), esophageal carcinoma (ESCA), glioblastoma multiforme (GBM), head and neck squamous cell carcinoma (HNSC), low-grade glioma (LGG), liver hepatocellular carcinoma (LIHC), lung adenocarcinoma (LUAD), lung squamous cell carcinoma (LUSC), pancreatic adenocarcinoma (PAAD), renal cell carcinoma (RCC), skin cutaneous melanoma (SKCM), stomach adenocarcinoma (STAD), and uterine corpus endometrial carcinoma (UCEC). (c), Prognostic performance in each cancer type for the top three methods on Virchow2. Survival differences between high- and low-risk groups were assessed using a two-sided log-rank test. Other statistical comparisons were performed using a two-sided Wilcoxon signed-rank test, where * indicates $P < 0.05$, ** indicates $P < 0.01$, and *** indicates $P < 0.001$. All results are reported as mean \pm standard deviation based on five-fold cross-validation.

nostic performance across all pathology foundation models with mean C-Index of 0.655, 0.650, and 0.641 for UNI, H0, and GigaPath, respectively. In comparison, the classical ABMIL method showed consistently lower performance, with mean C-Index of 0.604, 0.610, 0.587, and 0.614 on UNI, H0, GigaPath, and Virchow2, respectively. Overall, nnMIL improved the mean C-Index by 4.4–8.4% compared with the second-best MIL method under each foundation model, demonstrating superior survival prediction in pan-cancer settings.

To further assess the prognostic relevance of nnMIL, we investigated survival stratification using Kaplan–Meier (KM) curves based on predictions from nnMIL trained on Virchow2 (**Figure 4 (b)**). For each of the 16 cancer types, patients were divided into high- and low-risk groups according to the median predicted risk. The resulting KM curves showed clear and consistent separation between risk groups, with log-rank $P < 0.001$ for all cohorts except for LUSC ($P = 0.058$). The survival stratification was particularly pronounced in renal (RCC), esophageal (ESCA), endometrial (UCEC), and colorectal cancers (COADREAD), with hazard ratios larger than 3.0 and greater separation between predicted risk groups.

Finally, we performed a more detailed comparison of survival prediction performance within individual cancers (**Figure 4 (c)**). nnMIL achieved the highest C-Index in 15 out of 16 cancer types, demonstrating consistently superior performance over other MIL methods. The most notable improvements were observed in breast (BRCA), low-grade glioma (LGG), esophageal (ESCA), colorectal (COADREAD), and liver (LIHC) cancers, where nnMIL exceeded the second-best method by 6–15% in C-Index. In contrast, ABMIL and DSMIL generally yielded lower and more variable results across cohorts. Collectively, these analyses confirm that nnMIL provides more accurate and robust survival prediction across a wide range of tumor types.

Generalizability of prognostic models in external validation

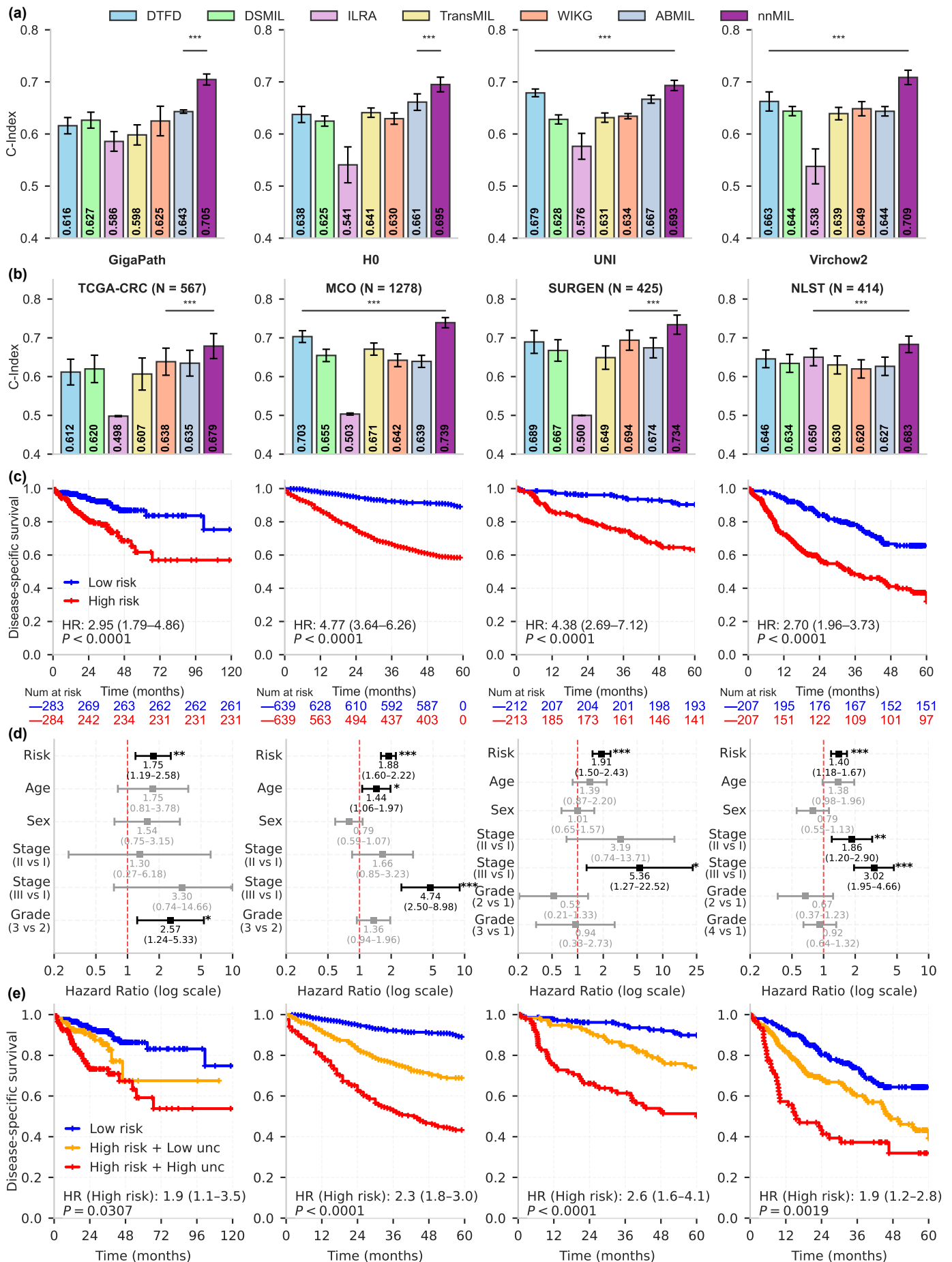


Figure 5: Generalizability of prognostic models in external validation. (a), Average performance of nnMIL and comparative methods across four independent external cohorts using four pathology foundation models (GigaPath, H0, UNI, and Virchow2). nnMIL consistently outperformed other MIL baseline methods across all foundation models. (b), Per-cohort survival prediction performance using Virchow2 features across three colorectal cancer cohorts (TCGA-CRC, MCO, and SURGEN) and one lung cancer cohort (NLST). (c), Kaplan–Meier survival analyses based on median-risk score in each external cohort, showing clear separation between high- and low-risk groups. (d), Multivariate Cox regression analyses controlling for clinical covariates, confirming that nnMIL provides independent prognostic value beyond conventional risk factors. (e), Kaplan–Meier survival analyses based on estimated uncertainty scores on high-risk group in each external cohort, showing clear separation between high- and low-uncertainty groups in high-risk score groups. Statistical significance for survival differences between high- and low-risk groups was assessed using a two-sided log-rank test. Other statistical comparisons were performed using a two-sided Wilcoxon signed-rank test, where * indicates $P < 0.05$, ** indicates $P < 0.01$, and *** indicates $P < 0.001$. All results are reported as mean and standard deviation, estimated from 1,000 bootstrap replicates.

Variations in tissue fixation, staining protocols, and slide digitization can lead to substantial heterogeneity in WSI appearance across institutions. Such differences can introduce significant distribution shifts that challenge the generalizability of computational pathology models. Moreover, survival prediction is inherently more challenging than disease classification, as it requires learning prognostic cues that are often subtle and confounded by clinical risk factors. Therefore, it is essential to rigorously evaluate model robustness and effectiveness across multiple independent external cohorts to assess its ability to generalize under diverse real-world clinical conditions. Here, we collected four colorectal cancer cohorts, including PLCO (with 1279 WSIs from 661 patients)⁴⁹, TCGA-CRC (with 596 WSIs from 567 patients)⁴⁷, MCO (with 1301 WSIs from 1278 patients)^{45,46} and SURGEN (with 425 WSIs from 425 patients)⁴⁴ and two non-small lung cancer cohorts, comprising PLCO (with 1455 WSIs from 470 patients)⁴⁹ and NLST (with 1143 WSIs from 414 patients)⁵⁰. PLCO is a multi-institutional study with sufficient follow-up, and therefore was used for model development in both cancers. All MIL methods were evaluated for disease-free survival prediction within each disease in the independent external cohorts.

Across four independent external cohorts, nnMIL achieved the highest concordance indices with all four pathology foundation features (Virchow2, GigaPath, UNI, and H0), outperforming other MIL methods such as ABMIL, DSMIL, TransMIL, and DTFD (**Figure 5 (a)**, **Extended Data Figure 1 (d)**, and **Extended Data Tables 13 to 16**). The performance gains were consistent across foundation models, with nnMIL surpassing the second-best method by 2–9% in C-Index ($P < 0.001$), indicating that its advantage is not dependent on a specific pretrained representation. Collectively, these results demonstrate that nnMIL delivers stronger survival discrimination than existing MIL approaches when evaluated on independent external cohorts.

We then performed a detailed per-cohort evaluation of survival prediction performance using Virchow2 as the feature extractor (**Figure 5 (b)**). Across all four external cohorts, nnMIL achieved the highest C-Index,

with performance gains of 4-10% ($P < 0.001$) compared with the second-best methods in each dataset (WIKG, DTFD, and ILRA). Notably, nnMIL maintained similarly strong performance across both disease types. In Kaplan–Meier analyses (**Figure 5 (c)**), predicted risk scores by nnMIL significantly stratified patients into distinct prognostic groups based on a median-risk threshold (all with log-rank $P < 0.0001$). Clear separation between high- and low-risk groups was observed across all external cohorts, with hazard ratios of 2.95 (95% CI: 1.79–4.86), 4.77 (95% CI: 3.64–6.26), and 4.38 (95% CI: 2.69–7.12) for the three CRC cohorts (TCGA-CRC, MCO, and SURGEN) and 2.70 (95% CI: 1.96–3.73) for the lung cohort (NLST). These results indicate that nnMIL achieves consistent survival stratification across external datasets and disease types.

We further examined whether the nnMIL risk score retained prognostic significance after controlling for clinical covariates, including age, sex, grade, and stage (**Figure 5 (d)**). In all external cohorts, the predicted risk scores by nnMIL remained a statistically significant predictor of disease-free survival, independent of conventional risk factors. Specifically, the hazard ratios estimates were 1.75 (95% CI: 1.19–2.58) for TCGA-CRC, 1.88 (95% CI: 1.60–2.22) for MCO, 1.91 (95% CI: 1.50–2.43) for SURGEN, and 1.40 (95% CI: 1.18–1.67) for NLST, with all $P < 0.01$. Collectively, these findings confirm that the nnMIL risk score provides independent prognostic value across both colorectal and lung cancer cohorts.

We finally investigated whether the model uncertainty scores generated by nnMIL could provide additional prognostic value beyond the risk score itself **Figure 5 (e)**. After stratifying patients by the nnMIL-derived risk score, the high-risk group was further subdivided according to estimated uncertainty into high-risk + low-uncertainty and high-risk + high-uncertainty subgroups (the hazard ratios in high-risk groups were 1.9, 2.3, 2.6 and 1.9 for TCGA-CRC, MCO, SURGEN and NLST, respectively, all $P < 0.05$). Across all external cohorts, the Kaplan–Meier curves showed a consistent pattern, with high-risk + high-uncertainty patients exhibiting the poorest survival, high-risk + low-uncertainty showing intermediate outcomes, and the low-risk group achieving the best prognosis. Consistently, scatter plots of predicted risk versus uncertainty (**Extended Data Figure 3**) demonstrated a positive association, indicating that uncertainty scores capture intrinsic heterogeneity within the high-risk population and complement risk-based prediction. Interestingly, the uncertainty scores did not further stratify patients among the low-risk population. Overall, these results suggest that integrating uncertainty estimates with risk scores could provide more refined prognostic stratification and highlights a subset of high-risk patients with high variability in model predictions and adverse outcomes.

Ablation experiments

We conducted six comparisons among the conventional ABMIL model trained with a batch size of one, the ABMIL with the nnMIL training strategies, and the complete nnMIL framework across four pathology foundation models (Virchow2, GigaPath, UNI, and H0, **Figure 1 (g)** and **Extended Data Table 17 and Figure 4**).

With these simple modifications, the nnMIL training strategy already enhances the stability and generalization of ABMIL across datasets and feature sources, suggesting that the training strategy can lead to promising performance gains. Building on this foundation, the full nnMIL, combining the modified MIL architecture and the rule-based configuration strategy, achieves strong cross-model consistency and the best overall results across 35 benchmarks covering three major categories of tasks: disease subtyping, biomarker detection, and prognosis prediction. Across all four foundation models, nnMIL consistently yields higher accuracy and substantially lower performance variance than existing ABMIL approaches, demonstrating that its streamlined architecture and rule-based training design jointly enable scalable, stable, and model-agnostic slide-level prediction.

We further evaluated the robustness of nnMIL to hyperparameter choices, focusing on hidden dimension, bag size, and inference stride. Across all tasks and datasets, nnMIL exhibits consistently stable behavior under broad parameter variations (**Extended Data Figure 4**). First, the hidden dimension shows a near-flat performance curve, with a broad optimum centered around 256. This flatness indicates that nnMIL does not depend on a finely tuned embedding size; instead, a wide range of moderate values (128–512) achieves nearly identical accuracy. In practice, selecting 256 serves as a strong default, preserving sufficient representational capacity while controlling memory usage, thus eliminating the need for extensive hyperparameter search. Similarly, model accuracy remains stable across different bag sizes, with only a mild saturation trend, where performance plateaus beyond the median bag length. This suggests that nnMIL effectively captures essential slide-level information even without large bag sizes. Finally, inference stride primarily affects computational cost rather than predictive accuracy. Varying the stride alters efficiency but produces negligible accuracy differences, enabling users to flexibly adjust inference speed without compromising performance. Together, these results highlight that nnMIL delivers high and reliable performance across a wide range of hyperparameter configurations, reinforcing its scalability, robustness, and ease of practical deployment.

Discussion

In this study, we proposed a novel perspective that focused on efficient training heavily, rather than MIL network design in the foundation-model era. Following this perspective, we introduce nnMIL, a simple yet generalizable framework for multiple instance learning (MIL) that bridges patch-level pathology foundation models with slide-level clinical prediction. Comprehensive evaluation across various clinical applications, including disease diagnosis and subtyping, molecular biomarker detection, and pan-cancer prognosis prediction, demonstrates that nnMIL significantly outperformed existing MIL methods while maintaining cross-model consistency and reliability.

A central challenge in MIL for computational pathology is the highly variable number of patches per slide, which has traditionally restricted model training to a batch size of one and prevents the use of advanced

optimization strategies. nnMIL resolves this issue by using a fixed-length bag size across slides, thereby enabling large and class-balanced mini-batches. Inspired by the rule-based design philosophy of nnU-Net³² for image segmentation, nnMIL follows a similar principle of distilling domain knowledge into explicit heuristic rules that guide model configuration, for example, determining an appropriate bag size from the dataset-level distribution. The use of larger batch sizes, suitable batch samplers, and well-chosen bag sizes generally leads to better performance. This design stabilizes gradients, improves convergence, and supports the integration of task-specific batch samplers to alleviate class imbalance^{51,52}. Further, nnMIL adopts a moderate dimension of hidden features to balance model capacity and regularization, which preserves the semantic features of pretrained foundation models without requiring additional projection layers as in existing MIL methods⁵³.

Across multiple slide-level tasks, including disease subtyping, biomarker detection, and prognosis prediction, nnMIL maintained strong generalization and consistently superior performance across cancer types, regardless of the pathology foundation models used for feature extraction. For molecular biomarker detection, models trained on one colorectal or brain tumor cohort generalized effectively to independent cohorts with distinct demographic and imaging characteristics. For prognosis prediction, nnMIL outperformed existing MIL methods in pan-cancer settings and is generalizable in independent validation cohorts for colorectal and lung cancer. Together, these results underscore nnMIL’s potential as an effective computational pathology tool in a wide range of clinical applications under real-world data variability.

One important advantage of nnMIL is the capability of uncertainty assessment for slide-level prediction. Traditional MIL methods fail to provide a confidence level of the prediction, which may hinder their utility for clinical decision support. nnMIL addresses this issue by computing uncertainty estimates through ensemble predictions. We show that the model uncertainty estimates align closely with actual reliability, where excluding samples with the highest uncertainty scores substantially improves performance on the remaining ones^{15,54}. This approach could be used to identify cases that may benefit from additional pathological review or advanced molecular testing, enabling selective referral in disease management. Further, we show that patients with higher uncertainty scores (i.e., higher variability in ensemble predictions) tend to have a worse prognosis, reinforcing the notion that intra-tumor morphological heterogeneity as a marker of aggressive biology and poor outcomes⁵⁵.

Although nnMIL does not introduce a new network architecture or loss function, we demonstrate that systematically optimizing the configuration of multiple instance learning (e.g., increasing batch sizes and applying different sampling) is sufficient to improve the performance of slide-level tasks in computational pathology significantly. The general design principle of nnMIL can be applied to other MIL methods and can also be combined with other task-specific loss functions (such as AUC loss, Kappa loss^{56,57}, which cannot be employed with a batch size of one). We have also shown that incorporating the nnMIL training strategy into

ABMIL further enhances its performance. Furthermore, this study is primarily conducted on publicly available benchmark datasets; validating nnMIL at a larger scale in real-world clinical environments will be essential to fully establish its translational readiness.

In conclusion, we introduce a training-centric perspective and present nnMIL, a new framework for multiple instance learning in computational pathology. By systematically optimizing the model configuration, nnMIL offers a simple and practical solution for making generalizable and uncertainty-aware predictions in clinically relevant tasks, paving the way for developing and deploying reliable AI models in real-world settings.

Methods

Design principles

nnMIL is a rule-driven, generalizable multiple instance learning (MIL) framework that connects patch-level foundation models to robust slide-level clinical predictions. Its design principles are: (i) *normalize the training interface* by converting variable-length bags into fixed-length sequences to enable large and diverse mini-batches; (ii) *regularize attention and preserve semantics* by computing attention in random feature subspaces during training while performing aggregation directly in the original embedding space; and (iii) *stabilize and quantify predictions* via subspace-ensemble inference that naturally estimates the uncertainty of slide-level predictions. Following a similar philosophy to nnU-Net (no-new U-Net)³² for image segmentation, we name our multiple instance learning approach as nnMIL (no-new MIL).

Architecture

The nnMIL architecture adopts a modified attention-based aggregator¹⁸ that transforms variable-length patch embeddings into fixed-size slide-level representations. Given a WSI containing N patches, each represented by a D -dimensional feature vector $\mathbf{x}_i \in \mathbb{R}^D$ extracted from a pathology foundation model, the aggregator computes attention weights α_i for each patch as:

$$\alpha_i = \frac{\exp(w^\top (\tanh(V\mathbf{x}'_i) \odot \sigma(U\mathbf{x}'_i)))}{\sum_{j=1}^N \exp(w^\top (\tanh(V\mathbf{x}'_j) \odot \sigma(U\mathbf{x}'_j)))} \quad (1)$$

where \mathbf{x}'_i denotes a randomly sampled subset of H dimensions (default $H = 256$) from the full D -dimensional embedding during training; $V, U \in \mathbb{R}^{H \times D}$ are learnable linear projections, $w \in \mathbb{R}^H$ is a scoring vector, \odot denotes element-wise multiplication, and \tanh and σ represent the hyperbolic tangent and sigmoid activation functions, respectively. This gated attention formulation combines additive and multiplicative interactions, enabling the model to capture non-linear dependencies and to learn discriminative patch-level importance. The slide-level representation $\mathbf{h} \in \mathbb{R}^D$ is obtained via attention-weighted aggregation:

$$\mathbf{h} = \sum_{i=1}^N \alpha_i \mathbf{x}_i \quad (2)$$

and the final prediction is produced by a linear classifier:

$$\hat{y} = \text{cls}(\mathbf{h}), \quad (3)$$

where cls denotes a linear projection layer that outputs class logits for classification tasks, continuous values for regression, or risk scores for survival analysis. By default, nnMIL employs a hidden dimension of $H = 256$

and a dropout rate of 0.25. These design choices strike a balance between model capacity and regularization, while the overall architecture remains minimal and easily transferable across diverse pathology foundation models.

Compared with conventional attention-based MIL architectures such as ABMIL¹⁸, nnMIL has two major distinctions. First, instead of projecting all feature channels through additional learned layers, nnMIL randomly samples a subset of feature dimensions during training to compute attention weights. This stochastic subspace sampling serves as an implicit regularizer, stabilizing optimization and improving generalization without increasing model complexity. Moreover, during inference, the full feature space is evenly partitioned into multiple overlapping subsets, and predictions from these subsets are averaged. This design provides an ensemble-like effect across feature subspaces, yielding more stable and uncertainty-aware slide-level predictions without requiring multiple trained models. Second, the aggregation operates directly on the original D -dimensional embeddings from the foundation model, rather than using an intermediate projection, thereby preserving the semantic integrity of pretrained features and minimizing unnecessary transformations.

Rule-based parameter design

For each dataset, nnMIL computes a compact data fingerprint consisting of: per-slide patch-count distribution (median, interquartile range, 5th/95th percentiles), magnification, embedding dimension D , class prevalence (classification), target range (regression), and event/censoring rates with time horizons (survival). Given this fingerprint, nnMIL derives a parameter configuration with: fixed bag size M , attention hidden size H (default 256), dropout (0.25), task-aware batch sampler and batch size, optimizer/scheduler, and inference stride for subspace coverage. To enable efficient large-batch training while handling variable-length bags, nnMIL introduces a two-level sampling strategy that partitions variable-length bags into uniform sub-bags.

Bag size during bag-level sampling. During training, each WSI is processed to a fixed bag size M determined from the dataset-level distribution of patch counts. Specifically, M is set to half the median number of patches per slide across the training set. For WSIs with more than M patches, a random subset of M patches is selected; for WSIs with fewer than M patches, zero-padding is applied. This ensures that all samples within a batch have uniform length, enabling efficient batch processing and gradient computation.

Hidden dim in hidden-level sampling. During the forward pass, the attention mechanism operates on a randomly sampled subset of H dimensions from the full D -dimensional feature space. This hidden-level sampling serves dual purposes: (1) it reduces computational cost during training while maintaining access to the full feature space through aggregation, and (2) it acts as a form of regularization, encouraging the model to learn robust representations that are not overly dependent on specific feature dimensions.

Batch sampler for mini-batch. To address class imbalance and improve data utilization across heterogeneous tasks, nnMIL employs task-aware batch samplers that ensure balanced representation within each mini-batch. For classification, the `BalancedBatchSampler` enforces approximately equal numbers of samples from each class, distributing any remainder in a round-robin fashion. For regression, the `RegressionBatchSampler` divides the target variable into bins and samples proportionally from each bin to achieve uniform coverage of the target range. For survival analysis, the sampler maintains balanced event rates and temporal distributions across batches. These task-aware samplers allow nnMIL to train with substantially larger batch sizes (typically 32 or higher) than conventional MIL methods restricted to a batch size of one, leading to smoother gradient updates, better data efficiency, and improved generalization.

Stride for sliding-window inference. During inference, the model employs a sliding-window approach to ensure comprehensive coverage of the feature space. The full D -dimensional feature space is divided into overlapping chunks of size H , with each chunk processed independently (the default stride S value is a quarter of H). Predictions are then averaged across all chunks (total number of $\frac{D-H}{S} + 1$) to produce the final slide-level prediction and uncertainty estimates.

Uncertainty estimation

nnMIL provides uncertainty estimates of the slide-level prediction via a sliding-window inference scheme that decomposes uncertainty into epistemic and aleatoric components^{33,34}. During evaluation, the full feature space is partitioned into K overlapping chunks of size H with a stride of $H/4$ (where $H = 256$). Each chunk is processed independently through the attention mechanism and classifier, producing a set of K predictions $\{\hat{y}_1, \hat{y}_2, \dots, \hat{y}_K\}$.

Classification tasks. For classification tasks, the final prediction is computed as the mean of the K logits:

$$\bar{y} = \frac{1}{K} \sum_{k=1}^K \hat{y}_k \quad (4)$$

The probability distribution for each chunk is obtained by applying the softmax function: $p_k = \text{softmax}(\hat{y}_k)$, and the average probability distribution is $\bar{p} = \frac{1}{K} \sum_{k=1}^K p_k$. The total uncertainty is quantified as the entropy of the average prediction:

$$H_{\text{total}} = H(\bar{p}) = - \sum_{c=1}^C \bar{p}_c \log(\bar{p}_c) \quad (5)$$

where C is the number of classes and \bar{p}_c is the average probability for class c . The aleatoric uncertainty (data

uncertainty) is computed as the average entropy across all chunks:

$$H_{\text{aleatoric}} = \frac{1}{K} \sum_{k=1}^K H(p_k) = -\frac{1}{K} \sum_{k=1}^K \sum_{c=1}^C p_{k,c} \log(p_{k,c}) \quad (6)$$

where $p_{k,c}$ is the probability of class c for chunk k . The epistemic uncertainty (model uncertainty) is quantified as the mutual information (MI) between the input and model parameters, which represents the difference between total and aleatoric uncertainty:

$$\text{MI} = H_{\text{total}} - H_{\text{aleatoric}} = H(\bar{p}) - \frac{1}{K} \sum_{k=1}^K H(p_k) \quad (7)$$

The mutual information captures the model’s uncertainty about the prediction, with higher values indicating greater epistemic uncertainty. This decomposition follows the information-theoretic interpretation where total uncertainty equals the sum of aleatoric and epistemic components. For binary and multi-class classification tasks, both epistemic (MI) and aleatoric ($H_{\text{aleatoric}}$) uncertainties can be computed and used for selective prediction or model interpretation. To simplify the results, we employed the ($H_{\text{aleatoric}}$) for slide-level interpretability.

Prognosis prediction tasks. For survival analysis using Cox proportional hazards models, the final risk score is computed using log-sum-exp aggregation across K chunks:

$$\eta = \log \left(\frac{1}{K} \sum_{k=1}^K \exp(\eta_k) \right) \quad (8)$$

where η_k is the risk score (log hazard ratio) from chunk k . The primary epistemic uncertainty measure is the variance of risk scores across chunks:

$$\text{Var}_{\text{risk}} = \frac{1}{K} \sum_{k=1}^K (\eta_k - \bar{\eta})^2 \quad (9)$$

where $\bar{\eta} = \frac{1}{K} \sum_{k=1}^K \eta_k$ is the mean risk score. For clinical interpretability, we also compute the uncertainty in predicted survival probabilities^{58,59}. Given the baseline survival function $S_0(t)$ estimated from the training data, the survival probability at time t for each chunk is:

$$S_k(t) = S_0(t)^{\exp(\eta_k)} \quad (10)$$

The uncertainty in survival probability prediction is then quantified as the standard deviation across chunks:

$$\text{Unc}_{S(t)} = \sqrt{\frac{1}{K} \sum_{k=1}^K (S_k(t) - \bar{S}(t))^2} \quad (11)$$

where $\bar{S}(t) = \frac{1}{K} \sum_{k=1}^K S_k(t)$ is the mean survival probability. For patients with multiple WSIs, the uncertainty is adjusted by dividing by $\sqrt{n_{\text{WSI}}}$ to account for the increased sample size:

$$\text{Unc}_{S(t)}^{\text{adj}} = \frac{\text{Unc}_{S(t)}}{\sqrt{n_{\text{WSI}}}} \quad (12)$$

This adjustment ensures that uncertainty estimates are comparable across patients with different numbers of WSIs. The variance-based uncertainty (Var_{risk}) directly measures epistemic uncertainty in the risk score, while the survival probability-based uncertainty ($\text{Unc}_{S(t)}$) provides a clinically interpretable measure of prediction confidence in terms of survival outcomes. Here, we used the $\text{Unc}_{S(t)}$ at the median time point of each dataset for model interpretation.

Training protocol

All models were trained using the AdamW optimizer⁶⁰ with a learning rate of 3×10^{-4} (1×10^{-4} for prognosis tasks) and weight decay of 10^{-4} . The learning rate was scheduled using a cosine annealing schedule with a warmup⁶¹ period of 5 epochs. Models were trained for up to 100 epochs with early stopping⁶² based on validation performance (patience of 10 epochs), and we employed the latest epoch checkpoint for final evaluation. The default batch size was 32 for all tasks using the cross-entropy, Cox loss, and mean squared error loss functions for classification, prognosis and regression tasks. All experiments used a fixed random seed of 42 for reproducibility. All parameters were automatically determined from the dataset and task. This rule-based configuration follows the design philosophy of nnU-Net³², where domain knowledge is distilled into explicit heuristic rules that guide model configuration.

Feature extraction

All preprocessing and patch feature extraction were performed within the CLAM toolbox¹⁹, which provides an integrated pipeline for tissue segmentation, patch sampling, and model-specific preprocessing. For each whole-slide image (WSI), tissue regions were automatically identified using Otsu thresholding followed by morphological closing and hole filling to remove artifacts and background. Non-overlapping tiles were then extracted from the detected tissue regions at $40\times$, $20\times$, or $10\times$ magnification (~ 0.25 , ~ 0.50 , or ~ 1.0 $\mu\text{m}/\text{pixel}$), corresponding to raw patch sizes of 1024×1024 , 512×512 , or 256×256 pixels, respectively. Each patch was resized according to the input resolution required by the downstream foundation model and subsequently passed through the model’s feature extractor to obtain patch-level embeddings. Four pathology foundation models were used: GigaPath⁵ (1,536-dimensional embeddings), H0⁸ (1,536-dimensional), UNI¹⁰ (1,024-dimensional), and Virchow2³⁷ (2,560-dimensional). The resulting embeddings and corresponding patch coordinates were stored in HDF5 format for downstream multiple instance learning.

Evaluation protocol

For disease classification and biomarker prediction tasks, models were evaluated using official data splits or widely used splits¹⁷ from the respective datasets. Performance was assessed using balanced accuracy (BACC), area under the receiver operating characteristic curve (AUC), and Cohen’s kappa coefficient, as appropriate for each task. For survival analysis, models were evaluated using 5-fold cross-validation or independent evaluation with patient-level stratification to ensure that all slides from the same patient were assigned to the same fold⁷. Performance was assessed using the concordance index (C-Index) for survival discrimination. Kaplan-Meier curves and log-rank tests were used to assess risk stratification. For tasks with multiple evaluation sets (e.g., external validation cohorts), models were trained on development sets and evaluated independently on external test sets. Statistical significance was assessed using paired t-tests or Wilcoxon signed-rank tests as appropriate, with $P < 0.05$ considered significant.

Baseline MIL methods

nnMIL was compared against six existing MIL methods: ABMIL (Attention-based MIL)¹⁸, DSMIL (Dual-stream MIL)²¹, TransMIL (Transformer-based MIL)²³, DTFD-MIL (Dual-task Feature Distillation MIL)²⁰, WIKG-MIL (Weakly-supervised Instance-level Knowledge Graph MIL)²⁴, and ILRA-MIL (Iterative low-rank attention)²². All baseline methods were implemented using publicly available implementations and trained with identical hyperparameters and data splits to ensure fair comparison⁶³. For these baseline methods that typically use batch size of one, we maintained this configuration; for ABMIL (with nnMIL) that support larger batch sizes, we used batch size 32 to match nnMIL’s training configuration.

Benchmark datasets

We comprehensively evaluated and benchmarked nnMIL using over 35 datasets and nearly 40,000 unique whole-slide images (WSIs) across three major clinical tasks: disease classification and subtyping, molecular biomarker detection, and prognosis prediction.

BCCC (disease subtyping). This dataset comprises 1,832 WSIs from excision specimens of cutaneous basal cell carcinomas collected at the Department of Pathology, Sahlgrenska University Hospital³⁸. It includes three classification tasks with binary, three-class, and five-class labels. The official split provides 1,435 WSIs (with 200 slides held out for validation) for training and 397 WSIs for testing. One low-quality WSI was excluded from the training set due to poor image quality.

BRACS (disease subtyping). This breast carcinoma subtyping dataset contains seven categories, including normal tissue and six lesion subtypes: pathological benign, usual ductal hyperplasia, flat epithelial atypia,

atypical ductal hyperplasia, ductal carcinoma in situ, and invasive carcinoma³⁹. A total of 547 WSIs are divided into training, validation, and testing sets containing 395, 65, and 87 slides, respectively.

EBRAINS (disease subtyping). This is a brain tumor subtyping benchmark dataset for computational pathology model evaluation⁴⁰. It contains 2,319 WSIs annotated with both coarse-grained (12-class) and fine-grained (30-class) subtype labels. Following established works^{9,29,30}, the dataset is divided into 1,151 training, 595 validation, and 573 testing slides.

IMP-CRC2024 (disease subtyping). This dataset includes 5,333 H&E-stained FFPE colorectal biopsy and polypectomy WSIs obtained from the digital archive of the IMP Diagnostics laboratory, Portugal⁴¹. It provides three tumor grading categories: non-neoplastic lesions, low-grade lesions, and high-grade lesions. We followed the official split, using 4,433 slides for model development (with 887 slides held out for validation) and 900 slides for testing.

PANDA (disease subtyping). This large-scale prostate cancer grading dataset contains 9,555 WSIs with seven ISUP grade categories from the Radboud University Medical Center and the Karolinska Institute⁴². For training and evaluation, we followed the widely adopted split comprising 7,647, 954, and 954 slides for training, validation, and testing, respectively.

BCNB (biomarker detection). This dataset consists of 1,058 H&E-stained FFPE WSIs from core-needle biopsies of early breast cancer⁴³. Each case is annotated with the protein expression status for three established biomarkers: ER (WT: 227, MUT: 831, where WT means negative status and MUT is positive status), PR (WT: 268, MUT: 790), and HER2 (WT: 781, MUT: 277). The dataset was split in a label-stratified manner into training, validation, and testing sets with a 60:20:20 ratio, resulting in 740, 106, and 212 slides, respectively.

BRAF and KRAS in CRC (biomarker detection). To further evaluate the generalizability of nnMIL in clinically actionable biomarker prediction, we focused on two key biomarkers, *BRAF* and *KRAS* mutations, across four large colorectal cancer (CRC) cohorts, totaling 2,711 patients. These included the Molecular and Cellular Oncology (MCO)^{45,46} cohort (1,490 patients), the SURGEN⁴⁴ cohort (799 patients), and the TCGA-CRC⁴⁷ cohort (501 patients). The SURGEN dataset (primary CRC) represents a recently released real-world cohort and was used as the internal development set. Trained models were externally validated on the MCO (archival resection cases from 1994–2010) and TCGA-CRC (primary CRC with genomic characterization) cohorts.

IDH in brain tumor (biomarker detection). To further assess the generalizability of nnMIL in clinically actionable biomarker prediction for brain tumors, we focused on the isocitrate dehydrogenase (IDH) mutation status across different tumor grades using three independent cohorts. These included the Medical University

of Vienna (MUV-IDH)⁴⁰ dataset (872 WSIs from 794 patients), TCGA-LGG⁴⁷ (842 WSIs from 489 patients), and TCGA-HGG⁴⁷ (834 WSIs from 376 patients), comprising a total of 2,548 WSIs from 1,659 patients. We trained nnMIL on the MUV-IDH dataset and externally evaluated its performance on the TCGA-LGG and TCGA-HGG cohorts.

Aneuploidy regression in TCGA (biomarker detection). We applied nnMIL to predict the continuous Aneuploidy Score from routine histopathology images. Model performance was evaluated using the TCGA pan-cancer dataset⁴⁸, which included 10,854 WSIs from 8,819 patients. Patients were split into training, validation, and testing sets following a 7:1:2 ratio. For this regression task, Pearson correlation was used as the primary evaluation metric.

Whole-genome doubling in TCGA (biomarker). We also applied nnMIL to classify whole-genome doubling (WGD) status from routine histopathology images⁴⁸. Performance was evaluated using the TCGA pan-cancer dataset with the same data split as the Aneuploidy regression task. Consistent with prior studies⁴⁸, we simplified this task to a binary classification of WGD-positive (samples with one or more WGD events) versus WGD-negative (no WGD).

Tumor mutational burden in TCGA (biomarker detection). We further used nnMIL to classify tumor mutational burden (TMB) from routine histopathology images⁴⁸. Following clinical practice, we formulated this task as a binary prediction using the clinically established threshold of 10 mutations per megabase (mut/Mb). Performance was evaluated on the TCGA pan-cancer dataset using cross-validation, as the number of TMB-high cases was limited.

Pan-cancer prognosis in TCGA (prognosis prediction). To evaluate the generalizability of nnMIL in survival prediction across diverse cancer types, we constructed a pan-cancer prognosis cohort using The Cancer Genome Atlas (TCGA) collection⁴⁷. This cohort includes 16 major cancer types: bladder urothelial carcinoma (BLCA, 368 patients, 117 events), breast invasive carcinoma (BRCA, 1,007 patients, 76 events), cervical squamous cell carcinoma and endocervical adenocarcinoma (CESC, 258 patients, 47 events), colorectal and rectal adenocarcinoma (COADREAD, 392 patients, 56 events), esophageal carcinoma (ESCA, 134 patients, 34 events), glioblastoma multiforme (GBM, 347 patients, 287 events), head and neck squamous cell carcinoma (HNSC, 378 patients, 103 events), low-grade glioma (LGG, 480 patients, 103 events), liver hepatocellular carcinoma (LIHC, 332 patients, 68 events), lung adenocarcinoma (LUAD, 419 patients, 101 events), lung squamous cell carcinoma (LUSC, 405 patients, 77 events), pancreatic adenocarcinoma (PAAD, 173 patients, 79 events), renal cell carcinoma (RCC, 716 patients, 131 events), skin cutaneous melanoma (SKCM, 350 patients, 144 events), stomach adenocarcinoma (STAD, 353 patients, 92 events), and uterine corpus endometrial carcinoma (UCEC, 490 patients, 52 events). After quality control and removal of duplicate or low-quality

slides, the dataset comprised 7,927 WSIs from 6,602 unique patients with available DSS time and censoring information. The dataset was organized into five-fold cross-validation splits with patient-level stratification (note that the 12.5% training set was held out for validation; in each fold, the training:validation:test splits with 7:1:2 ratio), ensuring that all WSIs from the same patient were assigned to the same fold. Survival labels were defined using disease-specific survival time and censoring indicators, and model performance was evaluated using the concordance index (C-Index) and Kaplan–Meier risk stratification.

Prognostic generalization in colorectal cancer (prognosis prediction). To evaluate prognostic generalization across external cohorts, we collected four colorectal cancer cohorts with disease-specific survival (DSS) endpoints. The PLCO (Prostate, Lung, Colorectal and Ovarian Cancer Screening Trial)⁴⁹ colorectal cohort served as the development set, comprising 1,279 WSIs from 661 patients with 298 events (45.1% event rate). The PLCO dataset was divided into training (1,009 WSIs from 528 patients) and validation (270 WSIs from 133 patients) sets. Three independent external cohorts were used for evaluation: MCO ($n=1,278$ patients with 1,301 WSIs, 321 events)^{45,46}, TCGA-CRC ($n=567$ patients with 596 WSIs, 79 events)⁴⁷, and SURGEN ($n=425$ patients with 425 WSIs, 95 events)⁴⁴. All models were trained on the PLCO training set and evaluated independently on each external cohort to assess cross-institutional generalizability. Survival labels were defined using observed DSS time and censoring indicators, and model performance was evaluated using the concordance index (C-Index), Kaplan–Meier risk stratification, and multivariable Cox regression adjusting for clinical covariates including age, sex, grade, and stage.

Prognostic generalization in non-small cell lung cancer (prognosis prediction). To evaluate prognostic generalization for lung cancer, we collected two lung cancer cohorts with DSS endpoints. The PLCO lung cohort⁴⁹ served as the development set, comprising 1,455 WSIs from 470 patients with 231 progression events (49.1% event rate). The dataset was divided into training (1,156 WSIs from 376 patients) and validation (299 WSIs from 94 patients) subsets. The NLST (National Lung Screening Trial)⁵⁰ cohort was used as an independent external test set, comprising 1,143 WSIs from 414 patients with 169 progression events (40.8% event rate). All models were trained on the PLCO training set and independently evaluated on NLST to assess cross-institutional generalizability. Survival labels were defined using observed DSS time and censoring indicators, and performance was assessed using the concordance index (C-Index), Kaplan–Meier risk stratification, and multivariable Cox regression analysis adjusting for clinical covariates.

Statistical analysis

All performance metrics were computed using standard implementations from scikit-learn (version 1.0+) and lifelines (version 0.27+) libraries. Confidence intervals for metrics were computed using 1,000 bootstrap iterations. For cross-validation experiments, metrics were computed per fold and then averaged across folds, with

standard deviations reported. Statistical comparisons between methods were performed using paired t-tests or Wilcoxon signed-rank tests.

Computing hardware and software

All experiments and analyses were conducted using Python (version 3.10.12) and PyTorch (version 2.6.0, CUDA 12.4) (<https://pytorch.org>), together with other open-source packages as required. Whole-slide image (WSI) processing was performed using OpenSlide (version 4.3.1), openslide-python (version 1.4.2), and CLAM¹⁹, along with their respective dependencies. For linear probe evaluation, statistical analysis, and visualization, we used several public machine-learning libraries, including Scikit-learn (version 1.6.1), Scikit-survival (version 0.24.0), and Matplotlib (version 3.10.0). Four publicly available tile-level pathology foundation models were employed for feature extraction: UNI (<https://huggingface.co/Mahmo odLab/UNI>), GigaPath (<https://huggingface.co/prov-gigapath/prov-gigapath>), Virchow2 (<https://huggingface.co/paige-ai/Virchow2>), and H-optimus-0 (<https://huggingface.co/bioptimus/H-optimus-0>). All training and inference experiments were executed on a high-performance computing cluster equipped with 8×48 GB NVIDIA L40 GPUs. Training time varied according to dataset size and model complexity, ranging from approximately 0.5 hours for small datasets (for example, BRACS with 547 WSIs) to 5 hours for large-scale datasets (for example, TCGA pan-cancer with 10,854 WSIs). Inference required approximately 0.1–0.5 seconds per WSI, depending on the number of patches per slide.

Data availability

All histopathology images and clinical annotations used for model development and evaluation are publicly available from the following sources: BCCC (<https://datahub.aida.scilifelab.se/10.23698/aida/bccc>), BRACS (<https://www.bracs.icar.cnr.it/>), EBRAINS (<https://doi.org/10.25493/WQ48-ZGX>), IMP-CRC (<https://rdm.inesctec.pt/dataset/nis-2023-008>), PANDA (<https://www.kaggle.com/c/prostate-cancer-grade-assessment/data>), BCNB (<https://bupt-ai-cz.github.io/BCNB>), MCO (<https://www.sredhconsortium.org/sredh-datasets/mco-study-whole-slide-image-dataset>), SURGEN (<https://www.ebi.ac.uk/biostudies/studies/S-BIAD1285>), PLCO (<https://cdas.cancer.gov/plco/>), NLST (<https://www.cancerimagingarchive.net/collection/nlst/>), and TCGA (<https://portal.gdc.cancer.gov>). All datasets are accessible to the research community under their respective data use agreements or institutional licenses.

Code availability

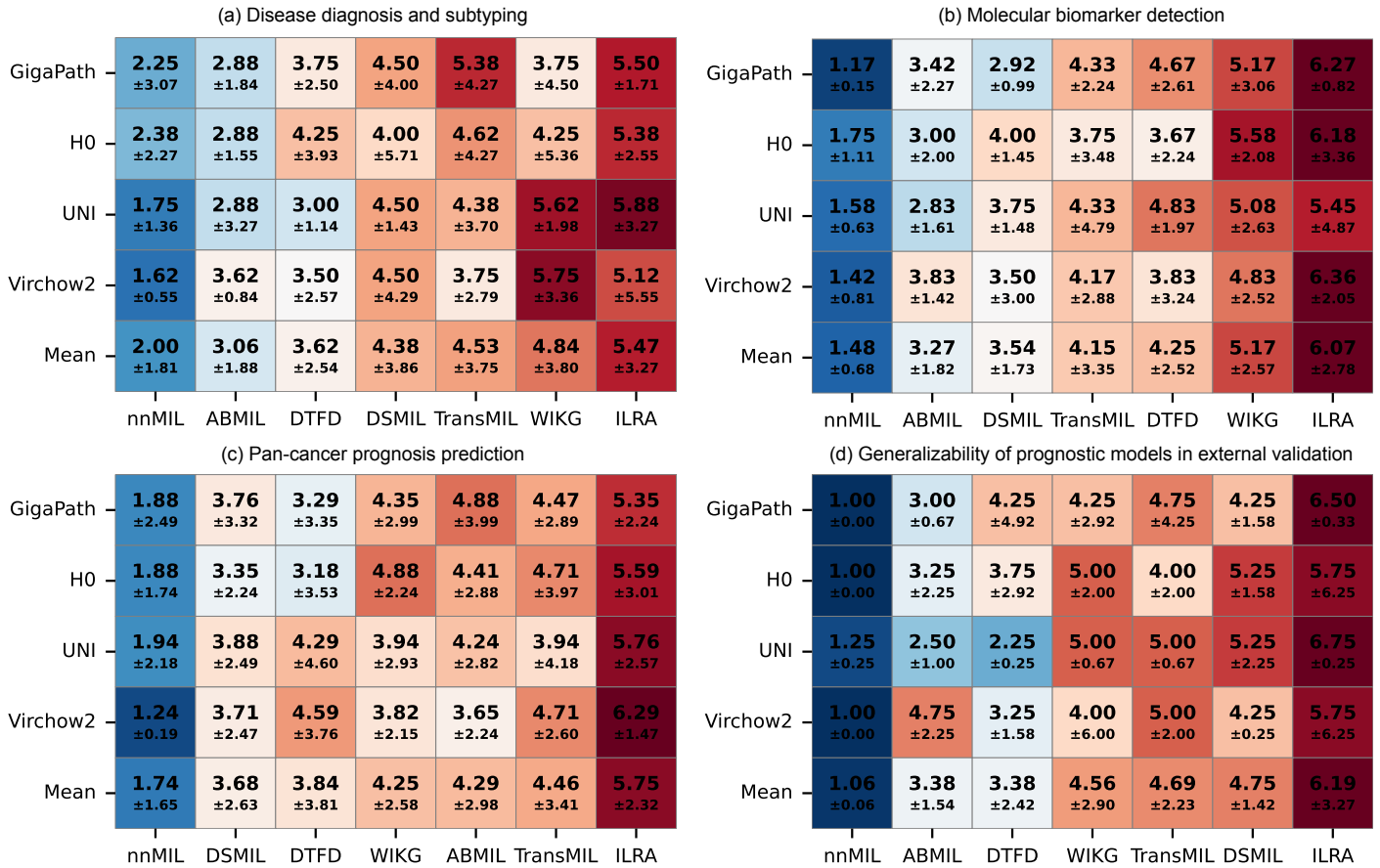
All implementations of this project, including training, inference, and evaluation pipelines as well as a usage tutorial, are publicly available at nnMIL.

Competing interests

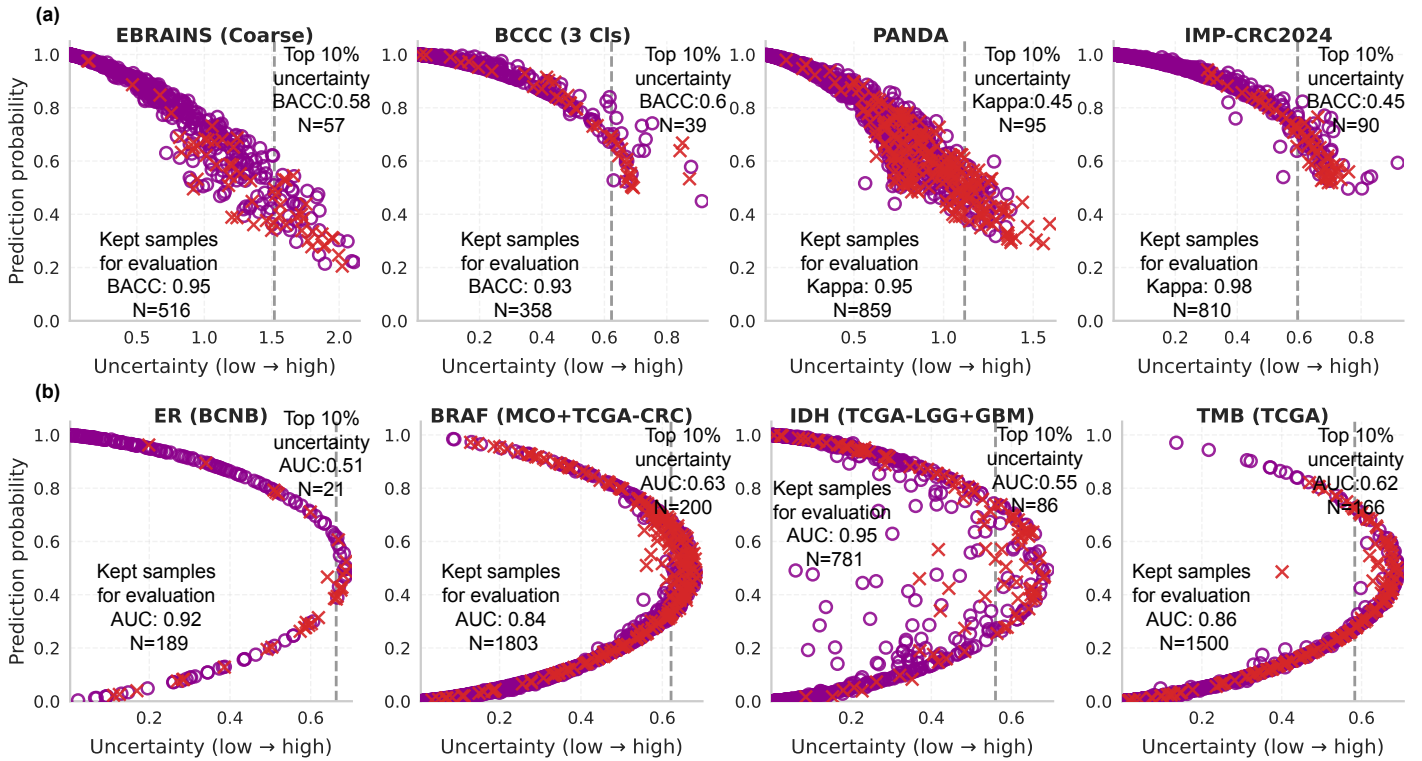
The authors declare no competing interests.

Acknowledgements

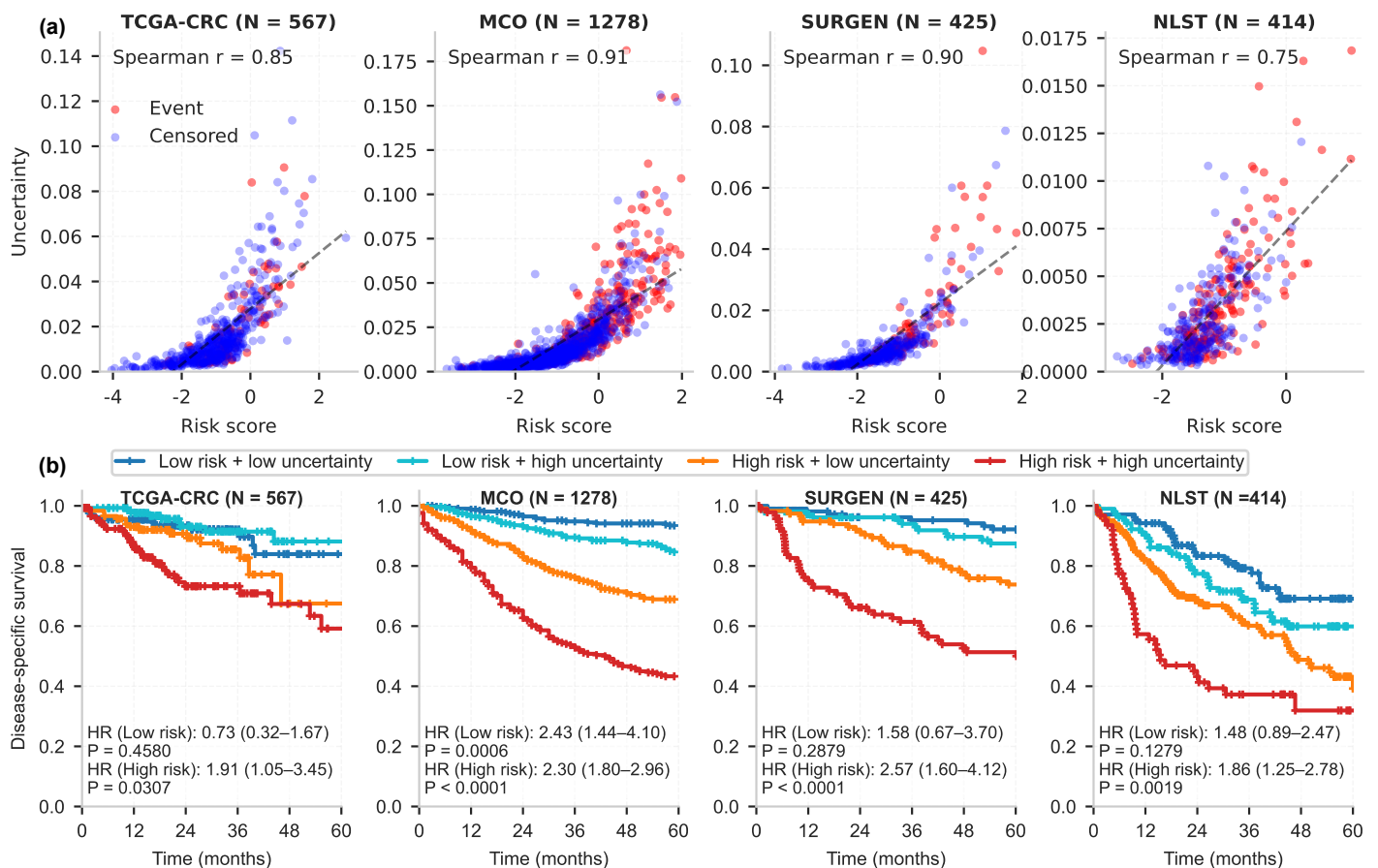
We acknowledge the BCCC³⁸, BCNB⁴³, BRACS³⁹, EBRAINS⁴⁰, IMP-CRS^{41,64}, PANDA⁴², MCO^{45,46}, SurGen⁴⁴, NLST⁵⁰, and TCGA⁴⁷ consortia for making their datasets publicly available. We further thank the research team⁴⁸ for providing aneuploidy scores and curating the whole-genome doubling and tumor mutational burden annotations.



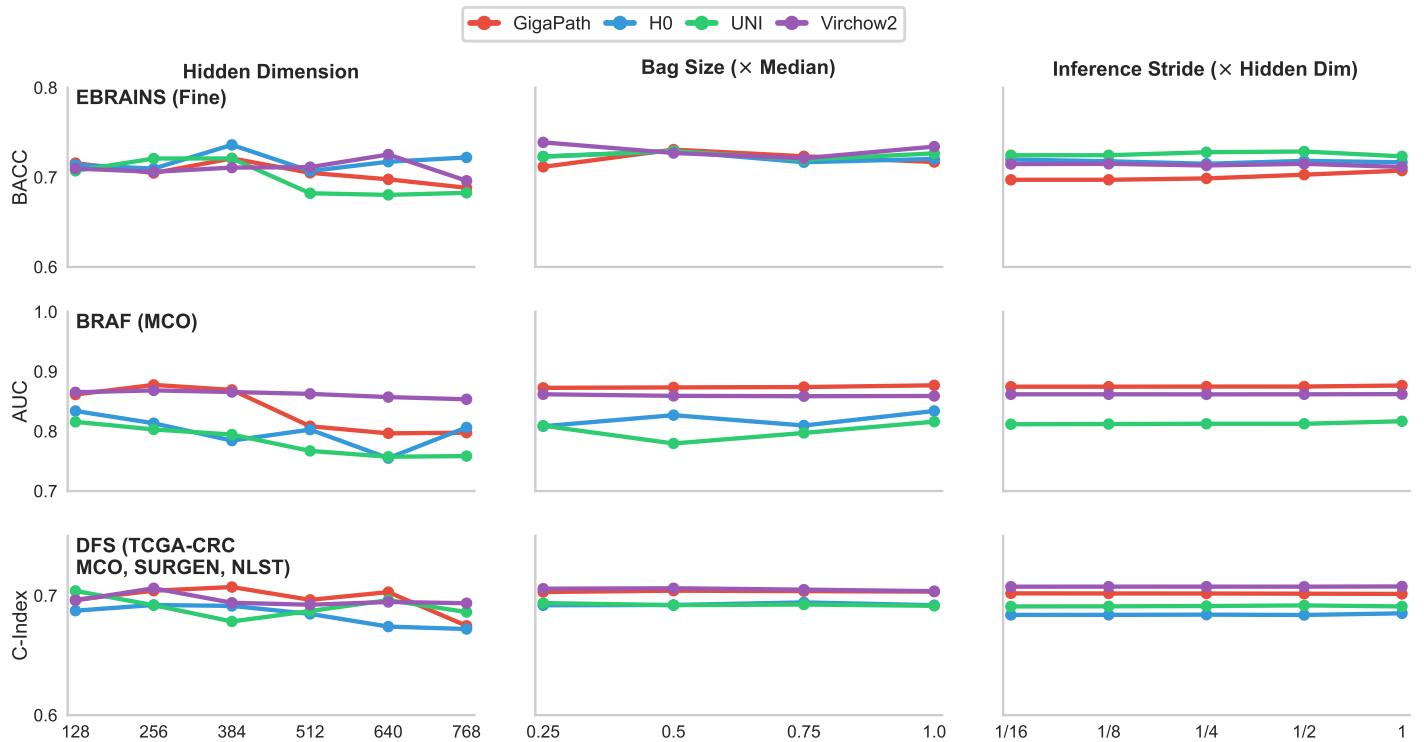
Extended Data Figure 1: Details ranking score across disease diagnosis and subtyping, molecular biomarker detection, pan-cancer prognosis prediction and generalizability of prognostic models in four external cohorts. All results are reported as mean \pm standard deviation.



Extended Data Figure 2: **The relationship between prediction score and estimated slide-level uncertainty.** (a), shows results for disease subtyping tasks, where uncertainty distinctly separates correct from incorrect predictions across EBRAINS, BCCC, PANDA, and IMP-CRC2024. (b), presents molecular biomarker detection tasks, including ER, BRAF, IDH, and TMB, showing that the same relationship between uncertainty and prediction accuracy is preserved, underscoring the model’s consistent calibration properties. Purple open circles indicate correctly classified cases, whereas orange crosses denote misclassified samples.



Extended Data Figure 3: **(a)**, Correlation between predicted risk and estimated uncertainty across external cohorts, demonstrating that uncertainty estimates are well calibrated and convey meaningful information about prediction confidence. **(b)**, Kaplan–Meier survival analyses based on estimated uncertainty scores on both low- and high-risk groups in each external cohort. Statistical significance of survival differences between high- and low-uncertainty groups in low- and high-risk groups was assessed using a two-sided log-rank test, respectively.



Extended Data Figure 4: **Ablation study of nnMIL.** Generalizability and stability analysis of nnMIL across key design parameters, including hidden dimension, bag size, and inference stride. nnMIL maintains robust and consistent performance across a wide range of hyperparameter settings, demonstrating strong resilience and practical generalizability. Statistical significance was assessed using a two-sided Wilcoxon signed-rank test, where * indicates $P < 0.05$, ** indicates $P < 0.01$, and *** indicates $P < 0.001$. All results are reported as mean and standard deviation, estimated from 1,000 bootstrap replicates.

Extended Data Table 1: Performance comparison of different MIL methods on disease classification and sub-typing tasks based on GigaPath. All results were evaluated using balanced accuracy (BACC), except for PANDA, which was assessed with Cohen’s Kappa. All results are reported as mean \pm standard deviation, estimated from 1,000 bootstrap replicates. Statistical significance was determined using a two-sided Wilcoxon signed-rank test, where * indicates $P < 0.05$, ** indicates $P < 0.01$, and *** indicates $P < 0.001$.

Dataset	DTFD	DSMIL	ILRA	TransMIL	WIKG	ABMIL	nnMIL
EBRAINS (Fine)	0.636 \pm 0.022	0.635 \pm 0.021	0.584 \pm 0.022	0.622 \pm 0.022	0.631 \pm 0.022	0.650 \pm 0.022	0.709 \pm 0.021 ***
EBRAINS (Coarse)	0.800 \pm 0.026	0.840 \pm 0.027	0.724 \pm 0.028	0.803 \pm 0.027	0.790 \pm 0.026	0.855 \pm 0.024	0.881 \pm 0.020 ***
PANDA	0.921 \pm 0.007	0.920 \pm 0.009	0.931 \pm 0.009	0.922 \pm 0.008	0.890 \pm 0.011	0.937 \pm 0.008 ***	0.934 \pm 0.007
IMP-CRC2024	0.947 \pm 0.008	0.862 \pm 0.013	0.944 \pm 0.008	0.941 \pm 0.008	0.948 \pm 0.008	0.947 \pm 0.008	0.950 \pm 0.007 ***
BCCC (2 Cls)	0.976 \pm 0.008 ***	0.974 \pm 0.008	0.956 \pm 0.010	0.953 \pm 0.011	0.964 \pm 0.009	0.956 \pm 0.011	0.965 \pm 0.009
BCCC (3 Cls)	0.897 \pm 0.016	0.837 \pm 0.018	0.881 \pm 0.016	0.910 \pm 0.015 ***	0.885 \pm 0.016	0.883 \pm 0.017	0.872 \pm 0.017
BCCC (5 Cls)	0.696 \pm 0.024	0.687 \pm 0.022	0.678 \pm 0.022	0.624 \pm 0.024	0.734 \pm 0.024 ***	0.714 \pm 0.021	0.705 \pm 0.021
BRACS	0.241 \pm 0.031	0.360 \pm 0.051	0.270 \pm 0.033	0.228 \pm 0.032	0.397 \pm 0.046	0.344 \pm 0.039	0.441 \pm 0.055 ***
Average	0.764 \pm 0.082	0.764 \pm 0.066	0.746 \pm 0.078	0.750 \pm 0.082	0.780 \pm 0.064	0.786 \pm 0.070	0.807 \pm 0.059

Extended Data Table 2: Performance comparison of different MIL methods on disease classification and sub-typing tasks based on H0. All results were evaluated using balanced accuracy (BACC), except for PANDA, which was assessed with Cohen’s Kappa. All results are reported as mean \pm standard deviation, estimated from 1,000 bootstrap replicates. Statistical significance was determined using a two-sided Wilcoxon signed-rank test, where * indicates $P < 0.05$, ** indicates $P < 0.01$, and *** indicates $P < 0.001$.

Dataset	DTFD	DSMIL	ILRA	TransMIL	WIKG	ABMIL	nnMIL
EBRAINS (Fine)	0.630 \pm 0.023	0.667 \pm 0.021	0.659 \pm 0.021	0.657 \pm 0.020	0.650 \pm 0.019	0.650 \pm 0.022	0.718 \pm 0.020 ***
EBRAINS (Coarse)	0.791 \pm 0.025	0.806 \pm 0.025	0.795 \pm 0.028	0.735 \pm 0.023	0.839 \pm 0.023	0.841 \pm 0.024	0.889 \pm 0.021 ***
PANDA	0.925 \pm 0.008	0.946 \pm 0.005 **	0.930 \pm 0.007	0.935 \pm 0.007	0.849 \pm 0.014	0.946 \pm 0.006	0.930 \pm 0.007
IMP-CRC2024	0.947 \pm 0.008	0.896 \pm 0.012	0.920 \pm 0.010	0.859 \pm 0.013	0.899 \pm 0.010	0.942 \pm 0.009	0.958 \pm 0.007 ***
BCCC (2 Cls)	0.974 \pm 0.008	0.972 \pm 0.008	0.949 \pm 0.010	0.968 \pm 0.008	0.976 \pm 0.008	0.976 \pm 0.008	0.973 \pm 0.008
BCCC (3 Cls)	0.894 \pm 0.016	0.866 \pm 0.018	0.873 \pm 0.017	0.896 \pm 0.016 *	0.890 \pm 0.016	0.894 \pm 0.016	0.892 \pm 0.016
BCCC (5 Cls)	0.722 \pm 0.023	0.685 \pm 0.024	0.665 \pm 0.025	0.737 \pm 0.020	0.755 \pm 0.020 *	0.742 \pm 0.022	0.752 \pm 0.020
BRACS	0.407 \pm 0.043	0.444 \pm 0.051 ***	0.330 \pm 0.046	0.392 \pm 0.050	0.384 \pm 0.045	0.394 \pm 0.049	0.434 \pm 0.055
Average	0.786 \pm 0.066	0.785 \pm 0.060	0.765 \pm 0.068	0.772 \pm 0.066	0.780 \pm 0.060	0.798 \pm 0.065	0.818 \pm 0.061

Extended Data Table 3: Performance comparison of different MIL methods on disease classification and sub-typing tasks based on UNI. All results were evaluated using balanced accuracy (BACC), except for PANDA, which was assessed with Cohen’s Kappa. All results are reported as mean \pm standard deviation, estimated from 1,000 bootstrap replicates. Statistical significance was determined using a two-sided Wilcoxon signed-rank test, where * indicates $P < 0.05$, ** indicates $P < 0.01$, and *** indicates $P < 0.001$.

Dataset	DTFD	DSMIL	ILRA	TransMIL	WIKG	ABMIL	nnMIL
EBRAINS (Fine)	0.644 \pm 0.022	0.627 \pm 0.020	0.605 \pm 0.022	0.635 \pm 0.022	0.614 \pm 0.022	0.656 \pm 0.020	0.724 \pm 0.020 ***
EBRAINS (Coarse)	0.798 \pm 0.026	0.790 \pm 0.027	0.774 \pm 0.027	0.785 \pm 0.026	0.756 \pm 0.024	0.844 \pm 0.025	0.913 \pm 0.019 ***
PANDA	0.928 \pm 0.007	0.922 \pm 0.009	0.925 \pm 0.010	0.920 \pm 0.008	0.902 \pm 0.010	0.938 \pm 0.009 ***	0.924 \pm 0.008
IMP-CRC2024	0.936 \pm 0.009	0.943 \pm 0.008	0.896 \pm 0.011	0.946 \pm 0.008	0.932 \pm 0.009	0.933 \pm 0.009	0.950 \pm 0.007 ***
BCCC (2 Cls)	0.975 \pm 0.008	0.958 \pm 0.010	0.957 \pm 0.011	0.965 \pm 0.010	0.970 \pm 0.009	0.976 \pm 0.008 ***	0.971 \pm 0.009
BCCC (3 Cls)	0.893 \pm 0.016	0.869 \pm 0.017	0.796 \pm 0.019	0.903 \pm 0.015 ***	0.874 \pm 0.016	0.872 \pm 0.017	0.896 \pm 0.016
BCCC (5 Cls)	0.707 \pm 0.023	0.717 \pm 0.022	0.722 \pm 0.022	0.695 \pm 0.022	0.685 \pm 0.022	0.725 \pm 0.022	0.736 \pm 0.021 ***
BRACS	0.414 \pm 0.053	0.407 \pm 0.049	0.303 \pm 0.036	0.336 \pm 0.043	0.363 \pm 0.048	0.366 \pm 0.041	0.444 \pm 0.053 ***
Average	0.787 \pm 0.063	0.779 \pm 0.062	0.747 \pm 0.072	0.773 \pm 0.071	0.762 \pm 0.065	0.789 \pm 0.070	0.820 \pm 0.059

Extended Data Table 4: Performance comparison of different MIL methods on disease classification and sub-typing tasks based on Virchow2. All results were evaluated using balanced accuracy (BACC), except for PANDA, which was assessed with Cohen’s Kappa. All results are reported as mean \pm standard deviation, estimated from 1,000 bootstrap replicates. Statistical significance was determined using a two-sided Wilcoxon signed-rank test, where * indicates $P < 0.05$, ** indicates $P < 0.01$, and *** indicates $P < 0.001$.

Dataset	DTFD	DSMIL	ILRA	TransMIL	WIKG	ABMIL	nnMIL
EBRAINS (Fine)	0.650 \pm 0.022	0.699 \pm 0.021	0.649 \pm 0.020	0.615 \pm 0.021	0.601 \pm 0.018	0.658 \pm 0.022	0.720 \pm 0.021 ***
EBRAINS (Coarse)	0.804 \pm 0.025	0.808 \pm 0.022	0.860 \pm 0.023	0.821 \pm 0.024	0.746 \pm 0.028	0.846 \pm 0.021	0.883 \pm 0.021 ***
PANDA	0.923 \pm 0.007	0.938 \pm 0.006 ***	0.908 \pm 0.010	0.927 \pm 0.008	0.914 \pm 0.007	0.934 \pm 0.008	0.935 \pm 0.007
IMP-CRC2024	0.945 \pm 0.008	0.944 \pm 0.008	0.930 \pm 0.009	0.952 \pm 0.007	0.929 \pm 0.008	0.941 \pm 0.008	0.964 \pm 0.006 ***
BCCC (2 Cls)	0.969 \pm 0.009	0.941 \pm 0.011	0.977 \pm 0.007 ***	0.969 \pm 0.009	0.964 \pm 0.010	0.967 \pm 0.009	0.975 \pm 0.008
BCCC (3 Cls)	0.909 \pm 0.016	0.864 \pm 0.018	0.814 \pm 0.018	0.892 \pm 0.016	0.909 \pm 0.015	0.899 \pm 0.016	0.908 \pm 0.015
BCCC (5 Cls)	0.747 \pm 0.023	0.722 \pm 0.022	0.712 \pm 0.024	0.777 \pm 0.022 ***	0.652 \pm 0.023	0.748 \pm 0.022	0.754 \pm 0.019
BRACS	0.400 \pm 0.046	0.341 \pm 0.042	0.255 \pm 0.029	0.368 \pm 0.047	0.383 \pm 0.038	0.399 \pm 0.048	0.409 \pm 0.051 ***
Average	0.793 \pm 0.065	0.782 \pm 0.064	0.763 \pm 0.077	0.790 \pm 0.070	0.762 \pm 0.069	0.799 \pm 0.066	0.818 \pm 0.063

Extended Data Table 5: Performance comparison of different MIL methods on molecular biomarker prediction tasks based on GigaPath. All results were evaluated using the area under the curve (AUC), except for Aneuploidy, which was assessed with Pearson’s correlation. All results are reported as mean \pm standard deviation, estimated from 1,000 bootstrap replicates. Statistical significance was determined using a two-sided Wilcoxon signed-rank test, where * indicates $P < 0.05$, ** indicates $P < 0.01$, and *** indicates $P < 0.001$.

Biomarker	DTFD	DSMIL	ILRA	TransMIL	WIKG	ABMIL	nnMIL
BCNB (ER)	0.819 \pm 0.038	0.854 \pm 0.031	0.833 \pm 0.033	0.847 \pm 0.033	0.859 \pm 0.029	0.889 \pm 0.026	0.902 \pm 0.023 ***
BCNB (HER2)	0.682 \pm 0.044	0.701 \pm 0.040	0.658 \pm 0.042	0.569 \pm 0.046	0.693 \pm 0.043	0.729 \pm 0.041	0.740 \pm 0.041 ***
BCNB (PR)	0.738 \pm 0.041	0.812 \pm 0.033	0.751 \pm 0.040	0.805 \pm 0.039	0.820 \pm 0.033	0.795 \pm 0.036	0.827 \pm 0.035 ***
BRAF (MCO)	0.717 \pm 0.021	0.842 \pm 0.014	0.508 \pm 0.009	0.777 \pm 0.019	0.662 \pm 0.022	0.631 \pm 0.019	0.875 \pm 0.013 ***
BRAF (TCGA-CRC)	0.645 \pm 0.044	0.775 \pm 0.036	0.501 \pm 0.022	0.755 \pm 0.040	0.772 \pm 0.031	0.743 \pm 0.037	0.777 \pm 0.038
KRAS (MCO)	0.575 \pm 0.016	0.595 \pm 0.016 ***	0.500 \pm 0.000	0.533 \pm 0.015	0.497 \pm 0.016	0.558 \pm 0.017	0.583 \pm 0.016
KRAS (TCGA-CRC)	0.606 \pm 0.026	0.612 \pm 0.025	0.502 \pm 0.005	0.563 \pm 0.025	0.468 \pm 0.026	0.603 \pm 0.025	0.640 \pm 0.025 ***
IDH (TCGA-LGG)	0.797 \pm 0.029	0.804 \pm 0.027	0.539 \pm 0.027	0.849 \pm 0.024 ***	0.786 \pm 0.027	0.824 \pm 0.026	0.840 \pm 0.026
IDH (TCGA-GBM)	0.854 \pm 0.044	0.841 \pm 0.035	0.576 \pm 0.059	0.846 \pm 0.040	0.747 \pm 0.077	0.828 \pm 0.042	0.902 \pm 0.028 ***
WGD (TCGA)	0.791 \pm 0.011	0.798 \pm 0.011	0.500 \pm 0.010	0.787 \pm 0.011	0.608 \pm 0.014	0.827 \pm 0.010	0.831 \pm 0.010 ***
TMB (TCGA)	0.788 \pm 0.019	0.810 \pm 0.018	0.799 \pm 0.017	0.796 \pm 0.019	0.763 \pm 0.017	0.824 \pm 0.017	0.844 \pm 0.016 ***
Aneuploidy (TCGA)	0.543 \pm 0.017	0.531 \pm 0.018	–	0.516 \pm 0.019	0.122 \pm 0.022	0.548 \pm 0.017	0.578 \pm 0.017 ***
Average	0.713 \pm 0.028	0.748 \pm 0.031	0.606 \pm 0.037	0.720 \pm 0.037	0.650 \pm 0.058	0.733 \pm 0.032	0.777 \pm 0.032

Extended Data Table 6: Performance comparison of different MIL methods on molecular biomarker prediction tasks based on H0. All results were evaluated using the area under the curve (AUC), except for Aneuploidy, which was assessed with Pearson’s correlation. All results are reported as mean \pm standard deviation, estimated from 1,000 bootstrap replicates. Statistical significance was determined using a two-sided Wilcoxon signed-rank test, where * indicates $P < 0.05$, ** indicates $P < 0.01$, and *** indicates $P < 0.001$.

Biomarker	DTFD	DSMIL	ILRA	TransMIL	WIKG	ABMIL	nnMIL
BCNB (ER)	0.877 \pm 0.030	0.875 \pm 0.026	0.862 \pm 0.032	0.838 \pm 0.034	0.859 \pm 0.031	0.865 \pm 0.031	0.899 \pm 0.025***
BCNB (HER2)	0.700 \pm 0.043	0.711 \pm 0.043	0.767 \pm 0.037***	0.655 \pm 0.041	0.696 \pm 0.044	0.745 \pm 0.042	0.735 \pm 0.039
BCNB (PR)	0.762 \pm 0.039	0.786 \pm 0.037	0.765 \pm 0.037	0.790 \pm 0.038	0.831 \pm 0.035***	0.801 \pm 0.034	0.823 \pm 0.036
BRAF (MCO)	0.771 \pm 0.017	0.750 \pm 0.018	0.520 \pm 0.015	0.832 \pm 0.016	0.708 \pm 0.021	0.876 \pm 0.014***	0.804 \pm 0.016
BRAF (TCGA-CRC)	0.736 \pm 0.038	0.780 \pm 0.033	0.527 \pm 0.031	0.790 \pm 0.033	0.686 \pm 0.037	0.807 \pm 0.034***	0.769 \pm 0.038
KRAS (MCO)	0.638 \pm 0.016	0.605 \pm 0.016	0.495 \pm 0.003	0.617 \pm 0.016	0.550 \pm 0.015	0.615 \pm 0.016	0.650 \pm 0.015***
KRAS (TCGA-CRC)	0.647 \pm 0.025	0.638 \pm 0.025	0.485 \pm 0.015	0.644 \pm 0.024	0.516 \pm 0.026	0.650 \pm 0.024	0.668 \pm 0.024***
IDH (TCGA-LGG)	0.832 \pm 0.025	0.852 \pm 0.023	0.561 \pm 0.028	0.840 \pm 0.024	0.773 \pm 0.029	0.818 \pm 0.025	0.868 \pm 0.023***
IDH (TCGA-GBM)	0.852 \pm 0.042	0.818 \pm 0.055	0.485 \pm 0.055	0.778 \pm 0.070	0.680 \pm 0.066	0.839 \pm 0.038	0.869 \pm 0.031***
WGD (TCGA)	0.813 \pm 0.011	0.812 \pm 0.010	0.559 \pm 0.012	0.824 \pm 0.010	0.599 \pm 0.014	0.827 \pm 0.010	0.836 \pm 0.010***
TMB (TCGA)	0.790 \pm 0.020	0.813 \pm 0.017	0.771 \pm 0.020	0.788 \pm 0.019	0.771 \pm 0.018	0.786 \pm 0.020	0.851 \pm 0.015***
Aneuploidy (TCGA)	0.559 \pm 0.016	0.480 \pm 0.018	–	0.608 \pm 0.016***	0.234 \pm 0.025	0.544 \pm 0.020	0.599 \pm 0.016
Average	0.748 \pm 0.027	0.743 \pm 0.032	0.618 \pm 0.040	0.750 \pm 0.026	0.658 \pm 0.048	0.764 \pm 0.029	0.779 \pm 0.027

Extended Data Table 7: Performance comparison of different MIL methods on molecular biomarker prediction tasks based on UNI. All results were evaluated using the area under the curve (AUC), except for Aneuploidy, which was assessed with Pearson’s correlation. All results are reported as mean \pm standard deviation, estimated from 1,000 bootstrap replicates. Statistical significance was determined using a two-sided Wilcoxon signed-rank test, where * indicates $P < 0.05$, ** indicates $P < 0.01$, and *** indicates $P < 0.001$.

Biomarker	DTFD	DSMIL	ILRA	TransMIL	WIKG	ABMIL	nnMIL
BCNB (ER)	0.859 \pm 0.033	0.876 \pm 0.026	0.884 \pm 0.029	0.842 \pm 0.034	0.867 \pm 0.026	0.868 \pm 0.030	0.908 \pm 0.022***
BCNB (HER2)	0.651 \pm 0.046	0.686 \pm 0.041	0.707 \pm 0.042	0.591 \pm 0.043	0.721 \pm 0.043***	0.687 \pm 0.043	0.709 \pm 0.041
BCNB (PR)	0.782 \pm 0.039	0.801 \pm 0.034	0.810 \pm 0.040	0.751 \pm 0.042	0.774 \pm 0.039	0.790 \pm 0.037	0.830 \pm 0.033***
BRAF (MCO)	0.711 \pm 0.019	0.730 \pm 0.020	0.507 \pm 0.010	0.826 \pm 0.016	0.528 \pm 0.024	0.847 \pm 0.015***	0.784 \pm 0.017
BRAF (TCGA-CRC)	0.786 \pm 0.028	0.760 \pm 0.033	0.528 \pm 0.021	0.795 \pm 0.037	0.573 \pm 0.038	0.800 \pm 0.035	0.823 \pm 0.031***
KRAS (MCO)	0.568 \pm 0.016	0.591 \pm 0.016	0.495 \pm 0.002	0.591 \pm 0.016	0.505 \pm 0.016	0.585 \pm 0.016	0.620 \pm 0.016***
KRAS (TCGA-CRC)	0.586 \pm 0.025	0.629 \pm 0.024	0.495 \pm 0.009	0.598 \pm 0.024	0.534 \pm 0.025	0.623 \pm 0.026	0.661 \pm 0.024***
IDH (TCGA-LGG)	0.809 \pm 0.027	0.821 \pm 0.026	0.650 \pm 0.029	0.814 \pm 0.024	0.812 \pm 0.025	0.819 \pm 0.026	0.846 \pm 0.024***
IDH (TCGA-GBM)	0.885 \pm 0.028***	0.766 \pm 0.065	0.681 \pm 0.072	0.767 \pm 0.058	0.738 \pm 0.077	0.851 \pm 0.041	0.842 \pm 0.044
WGD (TCGA)	0.795 \pm 0.011	0.804 \pm 0.011	0.515 \pm 0.010	0.796 \pm 0.011	0.687 \pm 0.013	0.818 \pm 0.010	0.824 \pm 0.010***
TMB (TCGA)	0.780 \pm 0.019	0.795 \pm 0.019	0.798 \pm 0.018	0.762 \pm 0.021	0.810 \pm 0.016	0.833 \pm 0.016***	0.827 \pm 0.017
Aneuploidy (TCGA)	0.554 \pm 0.017	0.540 \pm 0.016	–	0.605 \pm 0.016***	0.206 \pm 0.024	0.559 \pm 0.016	0.576 \pm 0.016
Average	0.730 \pm 0.032	0.733 \pm 0.028	0.643 \pm 0.041	0.728 \pm 0.028	0.646 \pm 0.052	0.757 \pm 0.030	0.771 \pm 0.028

Extended Data Table 8: Performance comparison of different MIL methods on molecular biomarker prediction tasks based on Virchow2. All results were evaluated using the area under the curve (AUC), except for Aneuploidy, which was assessed with Pearson’s correlation. All results are reported as mean \pm standard deviation, estimated from 1,000 bootstrap replicates. Statistical significance was determined using a two-sided Wilcoxon signed-rank test, where * indicates $P < 0.05$, ** indicates $P < 0.01$, and *** indicates $P < 0.001$.

Biomarker	DTFD	DSMIL	ILRA	TransMIL	WIKG	ABMIL	nnMIL
BCNB (ER)	0.887 \pm 0.028	0.881 \pm 0.024	0.876 \pm 0.026	0.886 \pm 0.026	0.882 \pm 0.026	0.885 \pm 0.029	0.904 \pm 0.024 ***
BCNB (HER2)	0.612 \pm 0.049	0.752 \pm 0.039	0.715 \pm 0.038	0.641 \pm 0.044	0.709 \pm 0.042	0.741 \pm 0.040	0.759 \pm 0.038 ***
BCNB (PR)	0.783 \pm 0.040	0.781 \pm 0.036	0.795 \pm 0.037	0.765 \pm 0.036	0.805 \pm 0.036	0.787 \pm 0.036	0.846 \pm 0.032 ***
BRAF (MCO)	0.691 \pm 0.020	0.820 \pm 0.016	0.499 \pm 0.004	0.762 \pm 0.020	0.674 \pm 0.018	0.713 \pm 0.019	0.866 \pm 0.014 ***
BRAF (TCGA-CRC)	0.691 \pm 0.042	0.805 \pm 0.028 ***	0.507 \pm 0.021	0.729 \pm 0.036	0.697 \pm 0.037	0.782 \pm 0.032	0.797 \pm 0.039
KRAS (MCO)	0.623 \pm 0.016	0.624 \pm 0.016	0.489 \pm 0.012	0.598 \pm 0.016	0.539 \pm 0.016	0.623 \pm 0.016	0.646 \pm 0.015 ***
KRAS (TCGA-CRC)	0.656 \pm 0.023 ***	0.636 \pm 0.025	0.488 \pm 0.022	0.558 \pm 0.026	0.514 \pm 0.026	0.634 \pm 0.024	0.623 \pm 0.025
IDH (TCGA-LGG)	0.814 \pm 0.026	0.820 \pm 0.026	0.653 \pm 0.030	0.835 \pm 0.024	0.716 \pm 0.032	0.821 \pm 0.025	0.849 \pm 0.023 ***
IDH (TCGA-GBM)	0.857 \pm 0.045	0.841 \pm 0.041	0.678 \pm 0.067	0.837 \pm 0.056	0.869 \pm 0.036	0.810 \pm 0.053	0.882 \pm 0.033 ***
WGD (TCGA)	0.823 \pm 0.010	0.792 \pm 0.011	0.522 \pm 0.012	0.802 \pm 0.011	0.603 \pm 0.015	0.841 \pm 0.010	0.845 \pm 0.009 ***
TMB (TCGA)	0.836 \pm 0.017	0.854 \pm 0.015	0.799 \pm 0.019	0.836 \pm 0.016	0.841 \pm 0.015	0.832 \pm 0.017	0.876 \pm 0.013 ***
Aneuploidy (TCGA)	0.561 \pm 0.018	0.544 \pm 0.017	–	0.637 \pm 0.016 ***	0.129 \pm 0.020	0.561 \pm 0.018	0.630 \pm 0.015
Average	0.736 \pm 0.030	0.762 \pm 0.030	0.638 \pm 0.043	0.741 \pm 0.031	0.665 \pm 0.060	0.753 \pm 0.029	0.795 \pm 0.029

Extended Data Table 9: Performance comparison of different MIL methods on pan-cancer prognosis tasks based on GigaPath. All results were evaluated using the C-Index. All results are reported as mean \pm standard deviation across five-fold evaluations. Statistical significance was determined using a two-sided Wilcoxon signed-rank test, where * indicates $P < 0.05$, ** indicates $P < 0.01$, and *** indicates $P < 0.001$.

Cancer Type	DTFD	DSMIL	ILRA	TransMIL	WIKG	ABMIL	nnMIL
BLCA	0.571 \pm 0.054	0.532 \pm 0.071	0.569 \pm 0.060	0.511 \pm 0.094	0.558 \pm 0.015	0.483 \pm 0.068	0.571 \pm 0.054
BRCA	0.629 \pm 0.053	0.629 \pm 0.030	0.498 \pm 0.002	0.584 \pm 0.018	0.605 \pm 0.052	0.667 \pm 0.044	0.719 \pm 0.033 ***
CESC	0.557 \pm 0.052	0.537 \pm 0.151	0.519 \pm 0.091	0.489 \pm 0.085	0.413 \pm 0.118	0.507 \pm 0.112	0.591 \pm 0.093 ***
COADREAD	0.641 \pm 0.066	0.667 \pm 0.052	0.577 \pm 0.071	0.537 \pm 0.065	0.616 \pm 0.078	0.640 \pm 0.079	0.692 \pm 0.054 ***
ESCA	0.649 \pm 0.121	0.634 \pm 0.077	0.636 \pm 0.103	0.556 \pm 0.103	0.576 \pm 0.074	0.527 \pm 0.126	0.674 \pm 0.042 ***
GBM	0.560 \pm 0.039	0.540 \pm 0.055	0.558 \pm 0.047	0.527 \pm 0.053	0.548 \pm 0.046	0.527 \pm 0.034	0.573 \pm 0.046 ***
HNSC	0.594 \pm 0.048 ***	0.523 \pm 0.083	0.541 \pm 0.091	0.564 \pm 0.107	0.565 \pm 0.078	0.550 \pm 0.107	0.547 \pm 0.070
LGG	0.689 \pm 0.037	0.709 \pm 0.066	0.557 \pm 0.081	0.643 \pm 0.075	0.687 \pm 0.056	0.720 \pm 0.040	0.771 \pm 0.062 ***
LIHC	0.651 \pm 0.065	0.689 \pm 0.046	0.653 \pm 0.076	0.635 \pm 0.087	0.593 \pm 0.127	0.644 \pm 0.064	0.726 \pm 0.045 ***
LUAD	0.591 \pm 0.060	0.534 \pm 0.041	0.549 \pm 0.072	0.579 \pm 0.077	0.617 \pm 0.026 ***	0.536 \pm 0.045	0.565 \pm 0.058
LUSC	0.505 \pm 0.063	0.563 \pm 0.128	0.498 \pm 0.044	0.509 \pm 0.100	0.527 \pm 0.111	0.498 \pm 0.067	0.559 \pm 0.089
PAAD	0.591 \pm 0.050 ***	0.548 \pm 0.104	0.542 \pm 0.057	0.569 \pm 0.056	0.554 \pm 0.061	0.534 \pm 0.040	0.536 \pm 0.055
RCC	0.781 \pm 0.021	0.763 \pm 0.028	0.512 \pm 0.017	0.768 \pm 0.035	0.743 \pm 0.043	0.752 \pm 0.031	0.813 \pm 0.022 ***
SKCM	0.544 \pm 0.054	0.586 \pm 0.075	0.563 \pm 0.044	0.591 \pm 0.070	0.569 \pm 0.096	0.596 \pm 0.060	0.603 \pm 0.048 ***
STAD	0.575 \pm 0.022	0.613 \pm 0.033 ***	0.587 \pm 0.071	0.605 \pm 0.074	0.606 \pm 0.085	0.554 \pm 0.068	0.597 \pm 0.054
UCEC	0.715 \pm 0.102	0.685 \pm 0.075	0.534 \pm 0.049	0.643 \pm 0.134	0.616 \pm 0.080	0.639 \pm 0.137	0.717 \pm 0.058
Average	0.615 \pm 0.017	0.609 \pm 0.019	0.556 \pm 0.010	0.582 \pm 0.017	0.587 \pm 0.017	0.586 \pm 0.021	0.640 \pm 0.022

Extended Data Table 10: Performance comparison of different MIL methods on pan-cancer prognosis tasks based on H0. All results were evaluated using the C-Index. All results are reported as mean \pm standard deviation across five-fold evaluations. Statistical significance was determined using a two-sided Wilcoxon signed-rank test, where * indicates $P < 0.05$, ** indicates $P < 0.01$, and *** indicates $P < 0.001$.

Cancer Type	DTFD	DSMIL	ILRA	TransMIL	WIKG	ABMIL	nnMIL
BLCA	0.583 \pm 0.068***	0.525 \pm 0.043	0.527 \pm 0.052	0.519 \pm 0.086	0.528 \pm 0.081	0.535 \pm 0.068	0.552 \pm 0.046
BRCA	0.666 \pm 0.076	0.659 \pm 0.070	0.495 \pm 0.022	0.597 \pm 0.077	0.627 \pm 0.098	0.653 \pm 0.086	0.756 \pm 0.021***
CESC	0.585 \pm 0.049	0.575 \pm 0.155	0.468 \pm 0.052	0.538 \pm 0.075	0.461 \pm 0.142	0.548 \pm 0.132	0.643 \pm 0.075***
COADREAD	0.619 \pm 0.038	0.626 \pm 0.085	0.574 \pm 0.082	0.565 \pm 0.074	0.613 \pm 0.071	0.649 \pm 0.106	0.661 \pm 0.125***
ESCA	0.632 \pm 0.126	0.697 \pm 0.034***	0.649 \pm 0.063	0.605 \pm 0.118	0.655 \pm 0.113	0.629 \pm 0.087	0.644 \pm 0.085
GBM	0.541 \pm 0.047	0.563 \pm 0.042	0.553 \pm 0.029	0.533 \pm 0.040	0.560 \pm 0.034	0.538 \pm 0.048	0.589 \pm 0.040***
HNSC	0.589 \pm 0.113	0.580 \pm 0.077	0.551 \pm 0.041	0.614 \pm 0.089	0.587 \pm 0.066	0.571 \pm 0.067	0.623 \pm 0.082***
LGG	0.653 \pm 0.025	0.751 \pm 0.089	0.588 \pm 0.112	0.676 \pm 0.072	0.708 \pm 0.032	0.746 \pm 0.058	0.765 \pm 0.064***
LIHC	0.650 \pm 0.074	0.654 \pm 0.102	0.535 \pm 0.093	0.630 \pm 0.103	0.572 \pm 0.111	0.648 \pm 0.051	0.727 \pm 0.070***
LUAD	0.558 \pm 0.045	0.572 \pm 0.064	0.497 \pm 0.093	0.491 \pm 0.061	0.570 \pm 0.093	0.557 \pm 0.052	0.534 \pm 0.033
LUSC	0.565 \pm 0.079***	0.544 \pm 0.108	0.548 \pm 0.040	0.524 \pm 0.096	0.509 \pm 0.130	0.509 \pm 0.104	0.552 \pm 0.106
PAAD	0.610 \pm 0.060***	0.564 \pm 0.031	0.503 \pm 0.039	0.566 \pm 0.054	0.532 \pm 0.050	0.584 \pm 0.068	0.593 \pm 0.049
RCC	0.776 \pm 0.027	0.776 \pm 0.035	0.624 \pm 0.079	0.761 \pm 0.030	0.741 \pm 0.041	0.752 \pm 0.032	0.809 \pm 0.033***
SKCM	0.620 \pm 0.066	0.570 \pm 0.055	0.578 \pm 0.062	0.591 \pm 0.045	0.570 \pm 0.041	0.568 \pm 0.065	0.622 \pm 0.055**
STAD	0.518 \pm 0.014	0.634 \pm 0.040	0.636 \pm 0.079	0.673 \pm 0.037***	0.604 \pm 0.042	0.585 \pm 0.073	0.614 \pm 0.052
UCEC	0.714 \pm 0.070	0.692 \pm 0.061	0.539 \pm 0.056	0.718 \pm 0.063	0.631 \pm 0.082	0.708 \pm 0.098	0.725 \pm 0.082***
Average	0.617 \pm 0.016	0.624 \pm 0.018	0.554 \pm 0.012	0.600 \pm 0.018	0.592 \pm 0.018	0.611 \pm 0.018	0.651 \pm 0.019

Extended Data Table 11: Performance comparison of different MIL methods on pan-cancer prognosis tasks based on UNI. All results were evaluated using the C-Index. All results are reported as mean \pm standard deviation across five-fold evaluations. Statistical significance was determined using a two-sided Wilcoxon signed-rank test, where * indicates $P < 0.05$, ** indicates $P < 0.01$, and *** indicates $P < 0.001$.

Cancer Type	DTFD	DSMIL	ILRA	TransMIL	WIKG	ABMIL	nnMIL
BLCA	0.503 \pm 0.051	0.537 \pm 0.049	0.546 \pm 0.076	0.507 \pm 0.079	0.563 \pm 0.096**	0.558 \pm 0.089	0.558 \pm 0.057
BRCA	0.622 \pm 0.043	0.677 \pm 0.041	0.520 \pm 0.027	0.582 \pm 0.080	0.632 \pm 0.050	0.666 \pm 0.044	0.792 \pm 0.034***
CESC	0.602 \pm 0.174	0.553 \pm 0.130	0.509 \pm 0.059	0.544 \pm 0.092	0.513 \pm 0.093	0.570 \pm 0.168	0.655 \pm 0.061***
COADREAD	0.685 \pm 0.068	0.645 \pm 0.061	0.523 \pm 0.046	0.597 \pm 0.098	0.632 \pm 0.075	0.638 \pm 0.068	0.691 \pm 0.034***
ESCA	0.576 \pm 0.084	0.665 \pm 0.123	0.656 \pm 0.080	0.639 \pm 0.081	0.642 \pm 0.141	0.602 \pm 0.074	0.685 \pm 0.084***
GBM	0.519 \pm 0.034	0.597 \pm 0.071***	0.567 \pm 0.035	0.530 \pm 0.057	0.589 \pm 0.051	0.547 \pm 0.037	0.577 \pm 0.054
HNSC	0.605 \pm 0.077	0.581 \pm 0.064	0.521 \pm 0.037	0.608 \pm 0.093	0.576 \pm 0.089	0.588 \pm 0.079	0.613 \pm 0.086
LGG	0.663 \pm 0.036	0.727 \pm 0.041	0.550 \pm 0.083	0.697 \pm 0.046	0.719 \pm 0.063	0.700 \pm 0.084	0.763 \pm 0.049***
LIHC	0.638 \pm 0.095	0.633 \pm 0.072	0.570 \pm 0.091	0.652 \pm 0.057	0.615 \pm 0.034	0.607 \pm 0.085	0.742 \pm 0.044***
LUAD	0.541 \pm 0.069	0.577 \pm 0.047	0.542 \pm 0.054	0.552 \pm 0.045	0.585 \pm 0.050***	0.538 \pm 0.068	0.575 \pm 0.050
LUSC	0.479 \pm 0.094	0.513 \pm 0.077	0.522 \pm 0.071	0.525 \pm 0.095	0.479 \pm 0.053	0.495 \pm 0.090	0.564 \pm 0.084***
PAAD	0.566 \pm 0.079	0.519 \pm 0.089	0.547 \pm 0.041	0.575 \pm 0.016***	0.557 \pm 0.087	0.563 \pm 0.059	0.526 \pm 0.074
RCC	0.791 \pm 0.022	0.784 \pm 0.033	0.587 \pm 0.067	0.708 \pm 0.043	0.743 \pm 0.029	0.763 \pm 0.019	0.805 \pm 0.027***
SKCM	0.584 \pm 0.091	0.555 \pm 0.067	0.548 \pm 0.080	0.602 \pm 0.071***	0.582 \pm 0.054	0.580 \pm 0.045	0.582 \pm 0.018
STAD	0.583 \pm 0.056	0.606 \pm 0.073	0.618 \pm 0.069	0.639 \pm 0.073***	0.626 \pm 0.056	0.598 \pm 0.028	0.626 \pm 0.059
UCEC	0.652 \pm 0.129	0.651 \pm 0.080	0.551 \pm 0.044	0.673 \pm 0.109	0.695 \pm 0.112	0.648 \pm 0.094	0.733 \pm 0.046***
Average	0.601 \pm 0.018	0.614 \pm 0.018	0.555 \pm 0.009	0.602 \pm 0.014	0.609 \pm 0.017	0.604 \pm 0.016	0.656 \pm 0.022

Extended Data Table 12: Performance comparison of different MIL methods on pan-cancer prognosis tasks based on Virchow2. All results were evaluated using the C-Index. All results are reported as mean \pm standard deviation across five-fold evaluations. Statistical significance was determined using a two-sided Wilcoxon signed-rank test, where * indicates $P < 0.05$, ** indicates $P < 0.01$, and *** indicates $P < 0.001$.

Cancer Type	DTFD	DSMIL	ILRA	TransMIL	WIKG	ABMIL	nnMIL
BLCA	0.527 \pm 0.058	0.540 \pm 0.033	0.531 \pm 0.051	0.529 \pm 0.089	0.553 \pm 0.092	0.572 \pm 0.041	0.585 \pm 0.069***
BRCA	0.616 \pm 0.079	0.673 \pm 0.091	0.499 \pm 0.001	0.611 \pm 0.070	0.636 \pm 0.095	0.636 \pm 0.056	0.757 \pm 0.019***
CESC	0.607 \pm 0.126	0.617 \pm 0.100	0.613 \pm 0.080	0.548 \pm 0.053	0.526 \pm 0.109	0.621 \pm 0.109	0.679 \pm 0.064***
COADREAD	0.645 \pm 0.099	0.706 \pm 0.032	0.506 \pm 0.015	0.602 \pm 0.060	0.647 \pm 0.092	0.657 \pm 0.056	0.726 \pm 0.050***
ESCA	0.632 \pm 0.129	0.591 \pm 0.109	0.601 \pm 0.086	0.595 \pm 0.077	0.607 \pm 0.161	0.593 \pm 0.067	0.687 \pm 0.074***
GBM	0.522 \pm 0.043	0.553 \pm 0.054	0.503 \pm 0.027	0.562 \pm 0.044	0.585 \pm 0.026	0.547 \pm 0.034	0.590 \pm 0.043***
HNSC	0.633 \pm 0.078***	0.565 \pm 0.043	0.502 \pm 0.063	0.599 \pm 0.059	0.587 \pm 0.054	0.600 \pm 0.069	0.619 \pm 0.077
LGG	0.701 \pm 0.040	0.701 \pm 0.040	0.507 \pm 0.014	0.613 \pm 0.101	0.711 \pm 0.062	0.699 \pm 0.063	0.746 \pm 0.031***
LIHC	0.713 \pm 0.075	0.667 \pm 0.039	0.611 \pm 0.113	0.680 \pm 0.035	0.654 \pm 0.076	0.643 \pm 0.044	0.727 \pm 0.049***
LUAD	0.511 \pm 0.038	0.532 \pm 0.059	0.505 \pm 0.048	0.539 \pm 0.051	0.562 \pm 0.065	0.550 \pm 0.050	0.589 \pm 0.038***
LUSC	0.496 \pm 0.104	0.555 \pm 0.068	0.494 \pm 0.047	0.525 \pm 0.052	0.509 \pm 0.081	0.553 \pm 0.060	0.591 \pm 0.092***
PAAD	0.534 \pm 0.059	0.565 \pm 0.067	0.576 \pm 0.054	0.657 \pm 0.084***	0.578 \pm 0.036	0.568 \pm 0.045	0.580 \pm 0.060
RCC	0.816 \pm 0.020***	0.793 \pm 0.022	0.513 \pm 0.011	0.756 \pm 0.027	0.768 \pm 0.021	0.786 \pm 0.012	0.814 \pm 0.016
SKCM	0.557 \pm 0.050	0.561 \pm 0.032	0.553 \pm 0.039	0.546 \pm 0.052	0.566 \pm 0.074	0.598 \pm 0.071	0.619 \pm 0.036***
STAD	0.603 \pm 0.064	0.661 \pm 0.045***	0.550 \pm 0.057	0.635 \pm 0.094	0.614 \pm 0.028	0.617 \pm 0.037	0.656 \pm 0.064
UCEC	0.671 \pm 0.101	0.729 \pm 0.052	0.508 \pm 0.016	0.695 \pm 0.089	0.705 \pm 0.079	0.595 \pm 0.050	0.758 \pm 0.082***
Average	0.611 \pm 0.021	0.625 \pm 0.019	0.536 \pm 0.011	0.606 \pm 0.016	0.613 \pm 0.018	0.614 \pm 0.015	0.670 \pm 0.018

Extended Data Table 13: Performance comparison of different MIL methods on generalization prognosis tasks based on Gigapath. All results were evaluated using the C-Index. All results are reported as mean \pm standard deviation, estimated from 1,000 bootstrap replicates. Statistical significance was determined using a two-sided Wilcoxon signed-rank test, where * indicates $P < 0.05$, ** indicates $P < 0.01$, and *** indicates $P < 0.001$.

Cohort	DTFD	DSMIL	ILRA	TransMIL	WIKG	ABMIL	nnMIL
TCGA-CRC	0.631 \pm 0.040	0.610 \pm 0.031	0.600 \pm 0.030	0.654 \pm 0.031	0.633 \pm 0.032	0.647 \pm 0.032	0.675 \pm 0.030***
MCO	0.597 \pm 0.016	0.587 \pm 0.016	0.522 \pm 0.007	0.543 \pm 0.017	0.535 \pm 0.017	0.647 \pm 0.016	0.728 \pm 0.014***
SURGEN	0.578 \pm 0.030	0.668 \pm 0.031	0.606 \pm 0.028	0.606 \pm 0.031	0.695 \pm 0.028	0.632 \pm 0.031	0.721 \pm 0.026***
NLST	0.658 \pm 0.024	0.641 \pm 0.021	0.615 \pm 0.022	0.590 \pm 0.023	0.637 \pm 0.022	0.647 \pm 0.024	0.694 \pm 0.022***
Average	0.616 \pm 0.016	0.627 \pm 0.015	0.586 \pm 0.019	0.598 \pm 0.019	0.625 \pm 0.028	0.643 \pm 0.003	0.705 \pm 0.011

Extended Data Table 14: Performance comparison of different MIL methods on generalization prognosis tasks based on H0. All results were evaluated using the C-Index. All results are reported as mean \pm standard deviation, estimated from 1,000 bootstrap replicates. Statistical significance was determined using a two-sided Wilcoxon signed-rank test, where * indicates $P < 0.05$, ** indicates $P < 0.01$, and *** indicates $P < 0.001$.

Cohort	DTFD	DSMIL	ILRA	TransMIL	WIKG	ABMIL	nnMIL
TCGA-CRC	0.665 \pm 0.033	0.652 \pm 0.028	0.499 \pm 0.001	0.656 \pm 0.038	0.628 \pm 0.032	0.643 \pm 0.031	0.667 \pm 0.032
MCO	0.638 \pm 0.017	0.618 \pm 0.016	0.500 \pm 0.000	0.657 \pm 0.016	0.608 \pm 0.016	0.695 \pm 0.014	0.728 \pm 0.013***
SURGEN	0.586 \pm 0.032	0.633 \pm 0.030	0.500 \pm 0.000	0.638 \pm 0.029	0.665 \pm 0.028	0.689 \pm 0.029	0.716 \pm 0.026***
NLST	0.661 \pm 0.023	0.597 \pm 0.024	0.664 \pm 0.024	0.613 \pm 0.024	0.617 \pm 0.024	0.618 \pm 0.026	0.668 \pm 0.022***
Average	0.638 \pm 0.016	0.625 \pm 0.010	0.541 \pm 0.034	0.641 \pm 0.009	0.630 \pm 0.011	0.661 \pm 0.016	0.695 \pm 0.014

Extended Data Table 15: Performance comparison of different MIL methods on generalization prognosis tasks based on UNI. All results were evaluated using the C-Index. All results are reported as mean \pm standard deviation, estimated from 1,000 bootstrap replicates. Statistical significance was determined using a two-sided Wilcoxon signed-rank test, where * indicates $P < 0.05$, ** indicates $P < 0.01$, and *** indicates $P < 0.001$.

Cohort	DTFD	DSMIL	ILRA	TransMIL	WIKG	ABMIL	nnMIL
TCGA-CRC	0.674 \pm 0.030	0.655 \pm 0.032	0.555 \pm 0.034	0.621 \pm 0.035	0.640 \pm 0.036	0.662 \pm 0.030	0.680 \pm 0.031***
MCO	0.704 \pm 0.014	0.630 \pm 0.016	0.615 \pm 0.015	0.630 \pm 0.016	0.625 \pm 0.016	0.667 \pm 0.015	0.727 \pm 0.014***
SURGEN	0.668 \pm 0.028	0.619 \pm 0.030	0.630 \pm 0.030	0.662 \pm 0.027	0.647 \pm 0.031	0.690 \pm 0.027***	0.681 \pm 0.028
NLST	0.670 \pm 0.022	0.608 \pm 0.023	0.505 \pm 0.003	0.614 \pm 0.023	0.624 \pm 0.024	0.648 \pm 0.023	0.684 \pm 0.021***
Average	0.679 \pm 0.007	0.628 \pm 0.009	0.576 \pm 0.025	0.631 \pm 0.009	0.634 \pm 0.005	0.667 \pm 0.008	0.693 \pm 0.010

Extended Data Table 16: Performance comparison of different MIL methods on generalization prognosis tasks based on Virchow2. All results were evaluated using the C-Index. All results are reported as mean \pm standard deviation, estimated from 1,000 bootstrap replicates. Statistical significance was determined using a two-sided Wilcoxon signed-rank test, where * indicates $P < 0.05$, ** indicates $P < 0.01$, and *** indicates $P < 0.001$.

Cohort	DTFD	DSMIL	ILRA	TransMIL	WIKG	ABMIL	nnMIL
TCGA-CRC	0.612 \pm 0.033	0.620 \pm 0.035	0.498 \pm 0.001	0.607 \pm 0.041	0.638 \pm 0.035	0.635 \pm 0.033	0.679 \pm 0.032***
MCO	0.703 \pm 0.015	0.655 \pm 0.016	0.503 \pm 0.003	0.671 \pm 0.016	0.642 \pm 0.016	0.639 \pm 0.016	0.739 \pm 0.013***
SURGEN	0.689 \pm 0.030	0.667 \pm 0.028	0.500 \pm 0.000	0.649 \pm 0.030	0.694 \pm 0.026	0.674 \pm 0.026	0.734 \pm 0.025***
NLST	0.646 \pm 0.023	0.634 \pm 0.023	0.650 \pm 0.022	0.630 \pm 0.023	0.620 \pm 0.024	0.627 \pm 0.024	0.683 \pm 0.021***
Average	0.663 \pm 0.018	0.644 \pm 0.009	0.538 \pm 0.034	0.639 \pm 0.012	0.649 \pm 0.014	0.644 \pm 0.009	0.709 \pm 0.014

Extended Data Table 17: Performance comparison of different MIL methods across all 35 tasks based on GigaPath, H0, UNI and Virchow2, respectively. All results are reported as mean \pm standard deviation, estimated from 1,000 bootstrap replicates or five-fold cross validation. Statistical significance was determined using a two-sided Wilcoxon signed-rank test, where * indicates $P < 0.05$, ** indicates $P < 0.01$, and *** indicates $P < 0.001$.

Foundation Model	Task	Performance (mean \pm s.d.)		
		ABMIL	ABMIL (with nnMIL)	nnMIL
GigaPath	Diagnosis	0.786 \pm 0.197	0.803 \pm 0.172	0.807 \pm 0.168
	Biomarker	0.733 \pm 0.113	0.744 \pm 0.116	0.778 \pm 0.113***
	Prognosis	0.600 \pm 0.079	0.635 \pm 0.077	0.654 \pm 0.081***
H0	Diagnosis	0.798 \pm 0.184	0.813 \pm 0.167	0.818 \pm 0.169*
	Biomarker	0.764 \pm 0.101	0.769 \pm 0.098	0.781 \pm 0.094
	Prognosis	0.622 \pm 0.068	0.647 \pm 0.069	0.660 \pm 0.075***
UNI	Diagnosis	0.788 \pm 0.190	0.800 \pm 0.187	0.820 \pm 0.166*
	Biomarker	0.757 \pm 0.107	0.752 \pm 0.104	0.771 \pm 0.099
	Prognosis	0.619 \pm 0.065	0.649 \pm 0.075	0.663 \pm 0.081***
Virchow2	Diagnosis	0.799 \pm 0.181	0.813 \pm 0.172	0.819 \pm 0.177**
	Biomarker	0.752 \pm 0.096	0.753 \pm 0.114	0.793 \pm 0.099**
	Prognosis	0.623 \pm 0.059	0.651 \pm 0.066	0.678 \pm 0.070***

References

1. Bera, K., Schalper, K. A., Rimm, D. L., Velcheti, V. & Madabhushi, A. Artificial intelligence in digital pathology—new tools for diagnosis and precision oncology. *Nature reviews Clinical oncology* **16**, 703–715 (2019).
2. Yates, J. & Van Allen, E. M. New horizons at the interface of artificial intelligence and translational cancer research. *Cancer Cell* **43**, 708–727 (2025).
3. Bhinder, B., Gilvary, C., Madhukar, N. S. & Elemento, O. Artificial intelligence in cancer research and precision medicine. *Cancer discovery* **11**, 900–915 (2021).
4. Van der Laak, J., Litjens, G. & Ciompi, F. Deep learning in histopathology: the path to the clinic. *Nature medicine* **27**, 775–784 (2021).
5. Xu, H. *et al.* A whole-slide foundation model for digital pathology from real-world data. *Nature* **630**, 181–188 (2024).
6. Wang, X. *et al.* A pathology foundation model for cancer diagnosis and prognosis prediction. *Nature* **634**, 970–978 (2024).
7. Xiang, J. *et al.* A vision–language foundation model for precision oncology. *Nature* 1–10 (2025).
8. Saillard, C. *et al.* H-optimus-0 (2024). URL <https://github.com/bioptimus/releases/tree/main/models/h-optimus/v0>.
9. Chen, R. J. *et al.* Towards a general-purpose foundation model for computational pathology. *Nature Medicine* **30**, 850–862 (2024).
10. Lu, M. Y. *et al.* A visual-language foundation model for computational pathology. *Nature Medicine* **30**, 863–874 (2024).
11. Vorontsov, E. *et al.* A foundation model for clinical-grade computational pathology and rare cancers detection. *Nature medicine* **30**, 2924–2935 (2024).
12. Ma, J. *et al.* Towards a generalizable pathology foundation model via unified knowledge distillation. *arXiv preprint arXiv:2407.18449* (2024).
13. Huang, Z., Bianchi, F., Yuksekogonul, M., Montine, T. J. & Zou, J. A visual–language foundation model for pathology image analysis using medical twitter. *Nature medicine* **29**, 2307–2316 (2023).
14. Wang, X. *et al.* Foundation model for predicting prognosis and adjuvant therapy benefit from digital pathology in gi cancers. *Journal of Clinical Oncology JCO–24* (2025).
15. Campanella, G. *et al.* Real-world deployment of a fine-tuned pathology foundation model for lung cancer biomarker detection. *Nature Medicine* 1–9 (2025).
16. Kondepudi, A. *et al.* Foundation models for fast, label-free detection of glioma infiltration. *Nature* **637**, 439–445 (2025).
17. Shao, D. *et al.* Do mil models transfer? *arXiv preprint arXiv:2506.09022* (2025).
18. Ilse, M., Tomczak, J. & Welling, M. Attention-based deep multiple instance learning. In *International conference on machine learning*, 2127–2136 (PMLR, 2018).
19. Lu, M. Y. *et al.* Data-efficient and weakly supervised computational pathology on whole-slide images. *Nature biomedical engineering* **5**, 555–570 (2021).

20. Zhang, H. *et al.* Dtf-d-mil: Double-tier feature distillation multiple instance learning for histopathology whole slide image classification. In *Proceedings of the IEEE/CVF conference on computer vision and pattern recognition*, 18802–18812 (2022).
21. Li, B., Li, Y. & Eliceiri, K. W. Dual-stream multiple instance learning network for whole slide image classification with self-supervised contrastive learning. In *Proceedings of the IEEE/CVF conference on computer vision and pattern recognition*, 14318–14328 (2021).
22. Xiang, J. & Zhang, J. Exploring low-rank property in multiple instance learning for whole slide image classification. In *The Eleventh International Conference on Learning Representations* (2023).
23. Shao, Z. *et al.* Transmil: Transformer based correlated multiple instance learning for whole slide image classification. *Advances in neural information processing systems* **34**, 2136–2147 (2021).
24. Li, J. *et al.* Dynamic graph representation with knowledge-aware attention for histopathology whole slide image analysis. In *Proceedings of the IEEE/CVF conference on computer vision and pattern recognition*, 11323–11332 (2024).
25. Neidlinger, P. *et al.* Benchmarking foundation models as feature extractors for weakly supervised computational pathology. *Nature Biomedical Engineering* 1–11 (2025).
26. Ma, J. *et al.* Pathbench: A comprehensive comparison benchmark for pathology foundation models towards precision oncology. *arXiv preprint arXiv:2505.20202* (2025).
27. El Nahhas, O. S. *et al.* From whole-slide image to biomarker prediction: end-to-end weakly supervised deep learning in computational pathology. *Nature Protocols* **20**, 293–316 (2025).
28. Chen, R. J. *et al.* Pan-cancer integrative histology-genomic analysis via multimodal deep learning. *Cancer cell* **40**, 865–878 (2022).
29. Vaidya, A. *et al.* Molecular-driven foundation model for oncologic pathology. *arXiv preprint arXiv:2501.16652* (2025).
30. Ding, T. *et al.* Multimodal whole slide foundation model for pathology. *arXiv preprint arXiv:2411.19666* (2024).
31. He, T. *et al.* Bag of tricks for image classification with convolutional neural networks. In *Proceedings of the IEEE/CVF conference on computer vision and pattern recognition*, 558–567 (2019).
32. Isensee, F., Jaeger, P. F., Kohl, S. A., Petersen, J. & Maier-Hein, K. H. nnu-net: a self-configuring method for deep learning-based biomedical image segmentation. *Nature methods* **18**, 203–211 (2021).
33. Lakshminarayanan, B., Pritzel, A. & Blundell, C. Simple and scalable predictive uncertainty estimation using deep ensembles. *Advances in neural information processing systems* **30** (2017).
34. Gal, Y. & Ghahramani, Z. Dropout as a bayesian approximation: Representing model uncertainty in deep learning. In *international conference on machine learning*, 1050–1059 (PMLR, 2016).
35. Goyal, P. *et al.* Accurate, large minibatch sgd: Training imagenet in 1 hour. *arXiv preprint arXiv:1706.02677* (2017).
36. Mandt, S., Hoffman, M. D. & Blei, D. M. Stochastic gradient descent as approximate bayesian inference. *Journal of Machine Learning Research* **18**, 1–35 (2017).
37. Zimmermann, E. *et al.* Virchow2: Scaling self-supervised mixed magnification models in pathology. *arXiv preprint arXiv:2408.00738* (2024).
38. Yacob, F. *et al.* Weakly supervised detection and classification of basal cell carcinoma using graph-transformer on whole slide images. *Scientific Reports* **13**, 7555 (2023).

39. Brancati, N. *et al.* Bracs: A dataset for breast carcinoma subtyping in h&e histology images. *Database* **2022**, baac093 (2022).
40. Roetzer-Pejrimovsky, T. *et al.* The digital brain tumour atlas, an open histopathology resource. *Scientific Data* **9**, 55 (2022).
41. Neto, P. C. *et al.* An interpretable machine learning system for colorectal cancer diagnosis from pathology slides. *NPJ precision oncology* **8**, 56 (2024).
42. Bulten, W. *et al.* Artificial intelligence for diagnosis and gleason grading of prostate cancer: the panda challenge. *Nature medicine* **28**, 154–163 (2022).
43. Xu, F. *et al.* Predicting axillary lymph node metastasis in early breast cancer using deep learning on primary tumor biopsy slides. *Frontiers in oncology* **11**, 759007 (2021).
44. Myles, C., Um, I. H., Marshall, C., Harris-Birtill, D. & Harrison, D. J. Surgen: 1020 h&e-stained whole slide images with survival and genetic markers. *arXiv preprint arXiv:2502.04946* (2025).
45. Ward, R. Mco study whole slide image collection (2015).
46. Jonnagaddala, J. *et al.* Integration and analysis of heterogeneous colorectal cancer data for translational research. In *Nursing Informatics 2016*, 387–391 (IOS Press, 2016).
47. Weinstein, J. N. *et al.* The cancer genome atlas pan-cancer analysis project. *Nature genetics* **45**, 1113–1120 (2013).
48. Taylor, A. M. *et al.* Genomic and functional approaches to understanding cancer aneuploidy. *Cancer cell* **33**, 676–689 (2018).
49. Gohagan, J. K. *et al.* The prostate, lung, colorectal and ovarian (plco) cancer screening trial of the national cancer institute: history, organization, and status. *Controlled clinical trials* **21**, 251S–272S (2000).
50. Team, N. L. S. T. R. The national lung screening trial: overview and study design. *Radiology* **258**, 243–253 (2011).
51. Hoffer, E., Hubara, I. & Soudry, D. Train longer, generalize better: closing the generalization gap in large batch training of neural networks. *Advances in neural information processing systems* **30** (2017).
52. Yang, Y. & Xu, Z. Rethinking the value of labels for improving class-imbalanced learning. *Advances in neural information processing systems* **33**, 19290–19301 (2020).
53. Luo, X. *et al.* Ensemble learning of foundation models for precision oncology. *arXiv preprint arXiv:2508.16085* (2025).
54. De Fauw, J. *et al.* Clinically applicable deep learning for diagnosis and referral in retinal disease. *Nature medicine* **24**, 1342–1350 (2018).
55. Sali, R., Jiang, Y., Attaranzadeh, A., Holmes, B. & Li, R. Morphological diversity of cancer cells predicts prognosis across tumor types. *JNCI: Journal of the National Cancer Institute* **116**, 555–564 (2024).
56. de La Torre, J., Puig, D. & Valls, A. Weighted kappa loss function for multi-class classification of ordinal data in deep learning. *Pattern Recognition Letters* **105**, 144–154 (2018).
57. Yuan, Z., Yan, Y., Sonka, M. & Yang, T. Large-scale robust deep auc maximization: A new surrogate loss and empirical studies on medical image classification. In *Proceedings of the IEEE/CVF International Conference on Computer Vision*, 3040–3049 (2021).
58. Cox, D. R. Regression models and life-tables. *Journal of the Royal Statistical Society: Series B (Methodological)* **34**, 187–202 (1972).

59. Kvamme, H. & Borgan, Ø. Continuous and discrete-time survival prediction with neural networks. *Life-time data analysis* **27**, 710–736 (2021).
60. Loshchilov, I. & Hutter, F. Decoupled weight decay regularization. *arXiv preprint arXiv:1711.05101* (2017).
61. Loshchilov, I. & Hutter, F. Sgdr: Stochastic gradient descent with warm restarts. *arXiv preprint arXiv:1608.03983* (2016).
62. Prechelt, L. Early stopping-but when? In *Neural Networks: Tricks of the trade*, 55–69 (Springer, 2002).
63. Ling, X. *et al.* Agent aggregator with mask denoise mechanism for histopathology whole slide image analysis. In *Proceedings of the 32nd ACM International Conference on Multimedia*, 2795–2803 (2024).
64. Neto, P. C. *et al.* imil4path: A semi-supervised interpretable approach for colorectal whole-slide images. *Cancers* **14**, 2489 (2022).